

UNIVERSITÀ
DEGLI STUDI
DI PADOVA



DEPARTMENT OF INFORMATION ENGINEERING

MASTER DEGREE IN BIOENGINEERING FOR NEUROSCIENCE

A novel Hidden Markov Model implementation for Brain-Computer Interface driven wheelchair

Supervisor

Prof. Luca Tonin

Candidate

Sebastiano Toniolo

Co-Supervisor

Ph.D. Piero Simonetto

ACADEMIC YEAR 2023-2024

Graduation date 12/12/2024

Abstract

Brain–Computer Interface (BCI) is a technology that promises to directly connect the human brain with external devices by translating user intentions into control signals. The primary aim of this technology is to develop applications that enhance the quality of life for individuals suffering from various motor-related pathologies. To achieve this, several approaches have been explored, including the integration of human intention with robotic intelligence, resulting in shared control systems.

In this thesis, an existing Motor Imagery EEG-based BCI, successfully used to drive an electric wheelchair, has been integrated with a Hidden Markov Model (HMM) framework to merge BCI and environmental data, creating a more robust shared control system. Additionally, this framework introduces the 'Rest' class, expanding the classifier's output from two ('Both Hands' and 'Both Feet') to three classes. This approach was tested on six healthy subjects in a simulated environment (ROS-Gazebo) using three different configurations. Enhanced performances were observed when environmental data were incorporated into the process. Based on the promising results of this preliminary work, further refinement and implementation could lead to higher stability and improved performances.

Contents

1	Introduction	6
1.1	Invasive and Non-invasive Acquisition Techniques	7
1.2	Foundation of Electroencephalography (EEG)	8
1.2.1	Cortical Areas and Electrodes	9
1.2.2	EEG signal and rhythms	11
1.3	Event Related Potential and Self-paced BCI	12
1.3.1	Human In The Loop	12
1.3.2	Event Related Potential BCI	14
1.3.3	Self-paced BCI	17
1.4	Thesis Objectives	24
2	Methods	25
2.1	Acquisition and Processing of EEG Data	25
2.2	Calibration and Feature Selection	28
2.3	Binary Gaussian Classifier	31
2.4	Hidden Markov Model and Traversability	31
2.4.1	HMM Structure	31
2.4.2	HMM states	32
2.4.3	Traversability and Transition Matrix	33
2.4.4	HMM Forward Step	35
2.5	Exponential Smoother	35
2.6	Evaluation Protocol	36
3	Results	38
3.1	Real Task Distributions	39
3.2	Performance and Traversability Effects	43
4	Discussion	47

A Appendix	50
A.1 Hidden Markov Model Foundation	50
A.1.1 Forward Algorithm	52
A.1.2 Other Algorithms	53
Bibliography	54

List of Figures

1.1	Example of invasive techniques electrodes	8
1.2	Piramidal cell dipole seen as BCI source	9
1.3	Diagram of human brain cortex lobes and functional areas	10
1.4	10-5 electrodes system	10
1.5	Representation of the different EEG rhythms.	12
1.6	BCI loop	13
1.7	Sound based P300 speller	16
1.8	Driving a wheelchair using SSVEP	16
1.9	Interaction ErrP	17
1.10	Reinforcement learning concept exploiting ErrP	17
1.11	Covert Visuospatial Attention example	18
1.12	Sensorimotor representation	19
1.13	Movement and MI task activation compared	20
1.14	Right and left hand MI controlateral activation	20
1.15	Imagination paradigm Graz MI BCI	20
1.16	Motor Imagery driven robotic pointer	21
1.17	Learning to control a BCI-driven wheelchair	23
1.18	Mutual learning results	23
1.19	Illustration of the general purposes of the thesis.	24
2.1	Acquisition setup	26
2.2	Electrodes map for MI BCI and Laplacian filter	27
2.3	Welch's algorithm	28
2.4	Calibration trial design	28
2.5	Feature selection MATLAB GUI	30
2.6	HMM used in the project	32
2.7	Ideal output probability distribution and HMM states PDFs	33
2.8	HMM transition matrix	35

2.9	Evaluation trial design	37
2.10	Obstacles and transition matrix during evaluation	37
3.1	C7 T_{off} distributions and confusion matrix	40
3.2	D6 T_{off} distributions and confusion matrix	40
3.3	G2 T_{off} distributions and confusion matrix	41
3.4	H5 T_{off} distributions and confusion matrix	42
3.5	H6 T_{off} distributions and confusion matrix	42
3.6	H7 T_{off} distributions and confusion matrix	43
3.7	Confusion matrix subject C7	44
3.8	Confusion matrix subject D6	44
3.9	Confusion matrix subject G2	45
3.10	Confusion matrix subject H7	45
3.11	Confusion matrix subject H5	45
3.12	Across subjects overall accuracy box-plot	46
4.1	BCI pipeline employed in this study	47
A.1	HMM example	52

1 Introduction

The Brain-Computer Interface (BCI) concept was first introduced in the early 1970s by Jacques J. Vidal [1], he showed the potential of using electroencephalographic signals in order to dialogue with a machine, opening the way for the study of neuroelectric events elicited by such interactions. Since then significant strides have been made in BCI research, driven by the refinement of digital systems that have greatly enhanced the efficiency and ease of acquiring, storing, and processing neurophysiological data. These advancements have not only expanded our understanding of brain activity, but have also led to the development of sophisticated BCI applications that are increasingly integrated into real-world environments [2]. In particular, the last decade has been highly productive in the field of BCI, both invasive and non invasive techniques have been extensively studied in order to convert the brain activity into control signals suitable for simulated environment or real robotic systems. The main purpose of BCI is then providing an alternative pathway of communication between the brain and computers especially beneficial for individuals with motor disabilities, such as Amyotrophic Lateral Sclerosis (ALS), Locked-in Syndrome (LIS), brainstem stroke, brain or spinal cord injury and many more.[3]. Different experiments have been conducted in order to develop assistive device that might enhance the quality of life of such individual. For example the BCI driven speller could allow the patient to communicate just by looking at a monitor [4], while the BCI driven wheelchair promises to enhance its mobility and autonomy [5].

In this first chapter the reader will go through the BCI foundations, including the nature of the involved signals and the various acquisition methods available, with a particular focus on Motor Imagery (MI) EEG-based BCI.

1.1 Invasive and Non-invasive Acquisition Techniques

The first crucial step in Brain-Computer Interface is acquiring useful cerebral signals. The methods available can be grouped in invasive and non-invasive techniques according to the level at which the signals are recorded [3].

The invasive approach is based on the implantation of electrodes arrays directly into the cortical tissues through out medical surgery. The electrodes type depends on the specific technique used, indeed it's possible to distinguish two main categories, namely Electrocor-ticography (ECoG) and Multielectrode arrays (MEAs) [6]. ECoG exploits the implantation of electrodes array subdurally on the arachnoidal surface of the brain without penetrating the cerebral tissue, typically these arrays consist of electrodes 2.3 mm in diameter placed 1 cm apart [7]. However the research is moving toward the miniaturization of ECoG arrays and new μ -ECoG arrays have been recently studied in order to improve the spatial resolution and reduce the invasiveness of the intervention [8]. An example of ECoG array is shown in Figure 1.1a. MEAs are electrode arrays that penetrate the cerebral tissue in order to offer extremely high spatial resolution. These electrodes are usually based on silicon and ceramics material and characterized by a high number of needles up to 100 needles per module [6]. Examples of MEAs are shown in Figure 1.1b. The invasive techniques allow to record both the electrical activity of single neurons and the summed neural activity from small populations of cells, leading to two types of signals, namely the single unit spikes and the local field potentials (LFP) respectively. These acquisition methods offer an high spatial resolution as well as an high temporal resolution compared to the non-invasive techniques. However the side effects of this approach are not neglectable, indeed beside the risk involved in the surgery, its important to consider the possible inflammation of the tissue that eventually leads to device encapsulation and formation of scar tissue on the cerebral cortex. Although important progress have been achieved in terms of biocompatibility, this still a challenge for further studies [6].

Non-invasive approaches allow to retrieve the activity of large population of neurons, and generally they are characterized by poor spatial resolution and a very good temporal resolution. These techniques exploit signals that can be acquired from outside the body such as variation of the electrical field, in case of Electroencephalography (EEG), changes in magnetic field, refers to the Magnetoencephalography (MEG), and hemodynamic responses, via functional magnetic resonance imaging and functional near-infrared spectroscopy [6] [3]. Characterized by low cost and high portability, EEG is the most suitable solution for non-invasive BCI application [3].

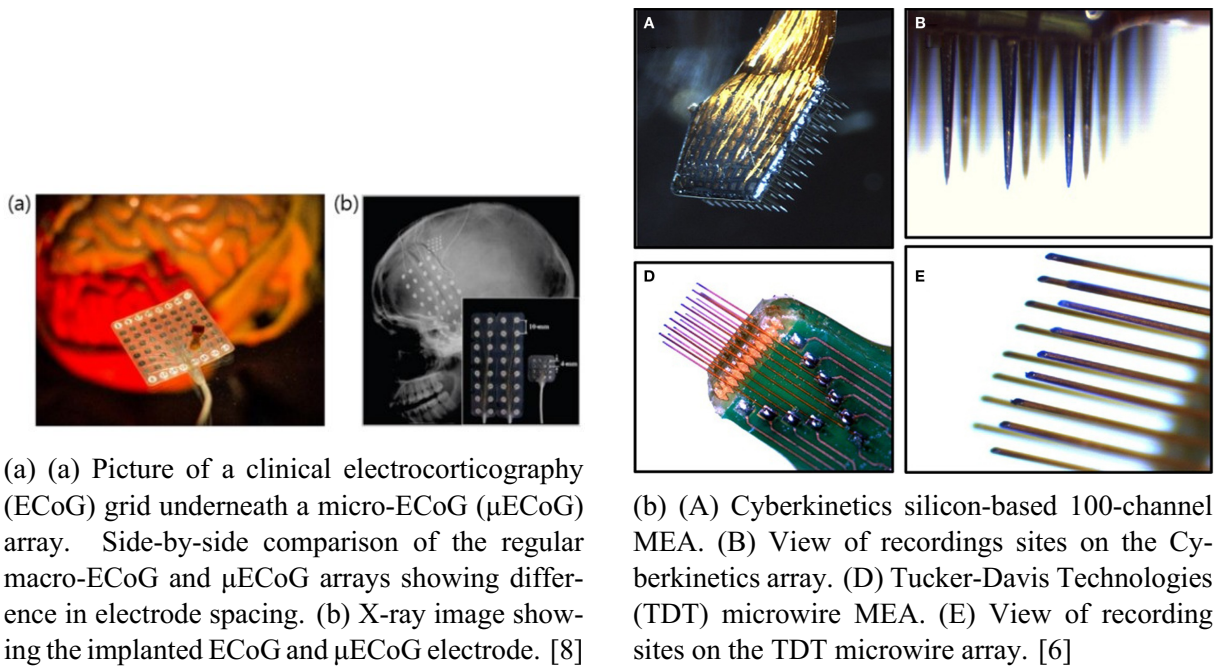


Figure 1.1: Example of invasive techniques electrodes

1.2 Foundation of Electroencephalography (EEG)

Human brain is populated by billions of neurons forming a dense network that can be divided into many subnetworks depending on the task performed. Neurons communicate with each other exploiting both chemical and electrical junctions, although they are characterized by different properties, the main process remain the same. A particular electrical signal known as Action Potential (AP) is actively conducted via the presynaptic neuron axon until it reaches the synaptic termination. Here the information encoded in the AP firing frequency is transmitted to the postsynaptic neuron as Post Synaptic Potential (PSP). The signal is then passively conducted via the postsynaptic neuron dendrites toward the cell body known as soma. At the soma level all the incoming signals are spatially and temporally integrated and, if a certain threshold is reached, an AP is generated in the axon, continuing the communication process. The continuous flowing of ionic current between cells lead to changes in the local extracellular potential and this phenomenon takes the name of Local Field Potential (LFP). Thanks to the conductive properties of the overlying tissues and the brain itself, it is possible to sense a distorted version of the LFP through electrodes mounted at the scalp level. LFP decays with the square of the distance from the source and, furthermore, the volume conductance of the head's tissues acts as a spatial smoother, hence only synchronous activity of large population of neurons can be detected by EEG electrodes [9]. Pyramidal cells are particular shaped neurons that populate the brain cortex and they are considered to be the main source of EEG. This is

because they are oriented perpendicular to the scalp surface and parallel to each other, allowing the integration of all the electrical dipoles resulting from their activity. As a result, an electric field is generated, which can propagate over long distances [9]. A sketch of the pyramidal cell's electrical dipole is shown in Figure 1.2.

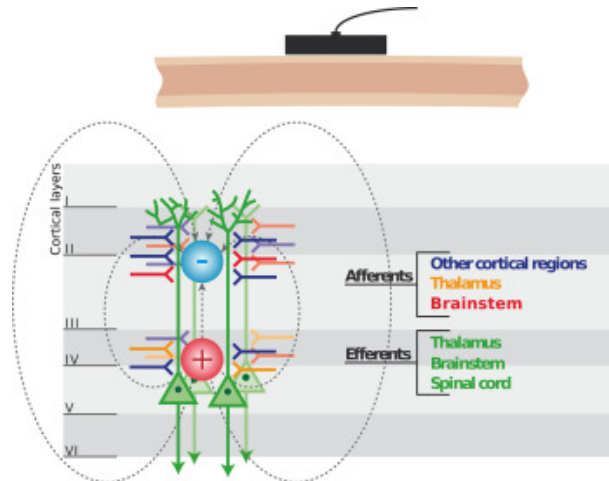


Figure 1.2: Pyramidal cell sketch seen as BCI source. The spatial and temporal dendritic integration of synaptic transmission leads to formation of electrical dipoles [9].

1.2.1 Cortical Areas and Electrodes

The signal retrieved via EEG reflect the major synchronous activity of the brain cortex, which is the outer part of the cerebrum. Five different anatomical part can be distinguished on the brain cortex, namely the frontal lobe, the parietal lobe, the occipital lobe and two temporal lobes. In addition to those anatomical lobes, several functional areas can be identified on the cerebral cortex. These areas are not strictly confined in the anatomical lobes boundaries and may vary among the two hemispheres. The so called functional areas are generally classified into three categories: sensory areas, which process the afferent sensory signals; the motor areas, which are involved in controlling voluntary movements; and associative areas, which are related to higher cognitive process [10]. A diagram is provided in Figure 1.3 for better understanding. In order to acquire useful signals from the aforementioned cortex partitions, a standard position system is used to ensure equal spacing between electrodes placed on the scalp. Following the 10-20 original system the electrodes are placed at 10% and 20% distances form the four anatomical landmarks, namely the nasion, inion, left and right preauricular points. More electrodes wise dense system, such as the 10-10 and the 10-5 system, have been designed exploiting the same principle [9]. Regardless of the system used, electrodes are named after the hemisphere and the lobe over which they are placed. The name begins with one or two letters that refer to the

anatomical lobe: F for frontal lobe, C for the central longitudinal line, P for the parietal lobe, O for the occipital lobe, and T for the temporal one. An additional character can be used to specify the proximity of the electrode to an other lobe; for example Fc stands for an electrode in the Frontal lobe but near the central line. Moreover the second character z means that the electrode lies on the sagittal line. After the letters comes a odd number for left hemisphere and an even number for the right one. [9]. An explicative sketch is provided in Figure 1.4. Over the years, several types of electrodes have been developed, which can be categorized into three main groups: gel-based, water-based, and dry electrodes. As the name suggests, the latter type doesn't require any addition of gel, or water, as a conductive bridge between the scalp and the actual electrode. Compared to the gel or water based electrodes, dry electrodes ensure a faster setup and eliminate the need to wash the head after use. However gel and water based electrodes offer greater stability and reliability, especially in terms of robustness against movement artifact [9]. The most suitable electrode type should be selected based on the experimental needs.

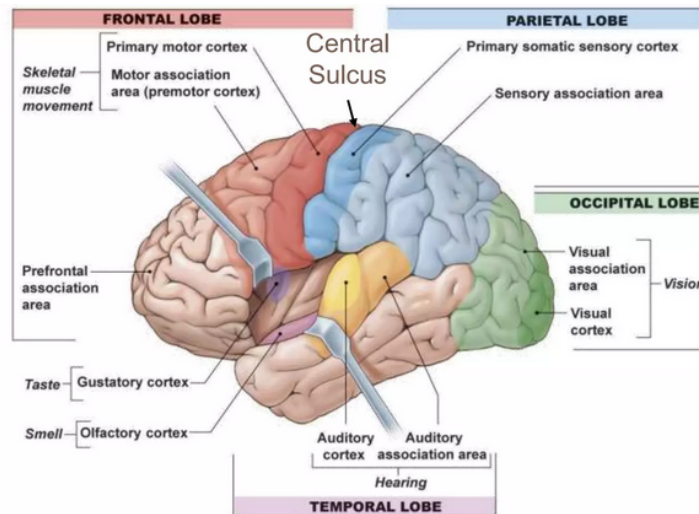


Figure 1.3: Diagram of human brain cortex lobes and functional areas [10].

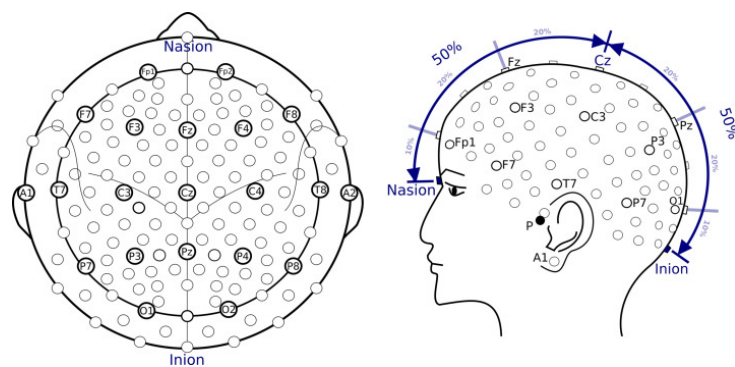


Figure 1.4: 10-5 electrode system, 10-20 are labeled and bold [9].

1.2.2 EEG signal and rhythms

EEG can be classified as a non-stationary stochastic signal, namely it exhibits random and unpredictable behavior that depends on initial condition. However, for short time windows, it can be assumed as stationary. EEG signal is characterized by a peak-to-peak amplitude typically under $100\mu\text{V}$ and a wide frequency spectrum, within which specific bands are associated with different physiological states [9]. A representation of the different EEG rhythms is shown in Figure 1.5. Although EEG signal is strongly individual specific, studying changes in the bands listed below can give valuable insight about the cognitive state of the subject and offer information about the mental task being performed.

- Delta (δ) rhythms (0.5-4 Hz) are the slowest EEG waves, they are characterized by high amplitude and are most prominent in the frontal and central regions of the brain during deep and restorative sleep. They play a critical role in processes such as memory consolidation and brain recovery [11].
- Theta (θ) rhythms (4-8 Hz) have moderate amplitude and are typically observed in the frontal and temporal regions during lighter sleep stages, relaxation, and meditative states, reflecting creativity and daydreaming [11].
- Alpha (α) rhythms (8-12 Hz) feature moderate amplitude and are most pronounced in the occipital and parietal regions when a person is awake but relaxed, often with closed eyes. They are associated with a state of calm attentiveness and readiness [11].
- Beta (β) rhythms (13-30 Hz) have lower amplitude and are prominent in the frontal and central regions. They are linked to active cognitive processes such as problem-solving, focused attention, and motor control, and they tend to increase with mental activity and alertness [11].
- Gamma (γ) rhythms (30-100 Hz) exhibit low amplitude and high frequency and are distributed across multiple brain regions, including the parietal and frontal lobes. They are involved in higher-order cognitive functions, such as sensory perception, working memory, and the integration of information across different brain areas [11].

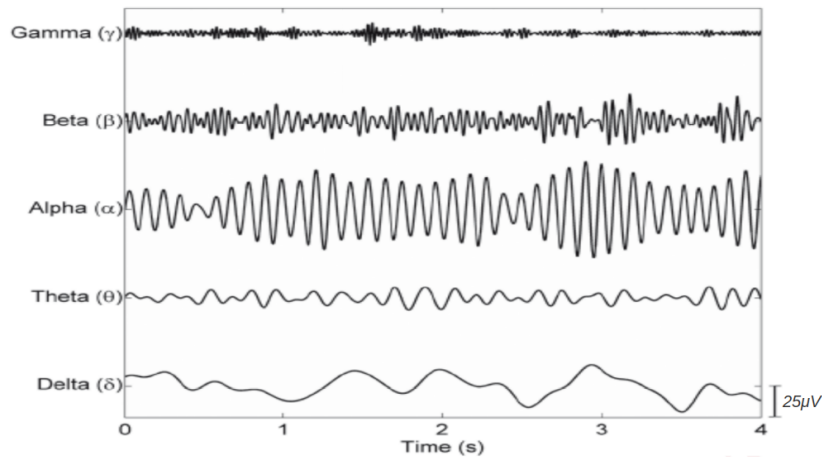


Figure 1.5: Representation of the different EEG rhythms.

1.3 Event Related Potential and Self-paced BCI

EEG-based BCI aims to retrieve the variation of the brain activity caused by a specific event in order to extrapolate the event itself and parse it into some kind of control signal. Based on the source of the event, two major types of EEG-based BCIs have been developed over the years: Event-Related Potential (ERP) and self-paced BCI. The first type, ERP, relies on exogenous stimuli that elicit responses in the subject's brain, while the second type, self-paced, is based on endogenous stimuli voluntarily controlled by the subject. Like other types of BCI, these methods require a loop architecture in which the subject plays a fundamental role [3].

1.3.1 Human In The Loop

Both the exogenous and the endogenous paradigms share the main loop architecture. Indeed, in both cases the EEG signal is acquired from the subject, then, the data collected are processed as needed in order to feed a classifier, whose output is used as control signal for eventual external actuators. The difference between the two types of non-invasive EEG based BCI consist on how the loop is closed. Namely, while for the exogenous paradigm the stimuli presented to the subject does not represent the output, but it is just an exogenous stimuli, in case of endogenous paradigm the stimuli is a proper feedback that resemble the classifier output. This closed loop architecture allows the subject to understand and actively control the ongoing process [3]. Further details about exogenous (ERP) and endogenous (self-paced) BCIs are provided in the following sections. Generally, beside the differences between these two types of paradigm, the BCI classifier has to be trained on subject specific features, as a result two different steps are required for building a proper BCI loop, namely, the Calibration (or Offline) loop and the Control

(or Online) loop [3] [12]. During the Calibration loop, data are acquired following specific trial protocols in order to extract subject specific features and train the classifier. In particular, the signal is processed to enhance the signal-to-noise ratio through out different methods. Spatial filters are, indeed, applied to reduce the low frequency components, which can interfere with the further analysis leading to bias in the interpretation of data. In addition, algorithm of projection into multidimensional space, such as principal component analysis (PCA) and independent component analysis (ICA), can be used for better explaining the variance of the signal and creating a new features space. Consequently, time and frequency based features can be extracted via algorithms like shape detection, band-pass filters, Fourier transform, wavelet decomposition, Welch's algorithm, and many others [3]. Once the features are extracted, a process of feature selection is performed in order to select only the most discriminant ones and reduce the dimensionality of the classifier [3]. Several machine learning and deep learning approaches have been tested in the field of BCI in order to create a stable and reliable classifier [13][14], which, once trained over the extracted features from the calibration data, can be used in the actual Control loop [12]. Finally, in the Control loop, the classifier is continuously fed with the samples retrieved by the subject, for delivering the needed control signals [12]. A sketch of the BCI loop is provided in Figure 1.6 for better understanding.

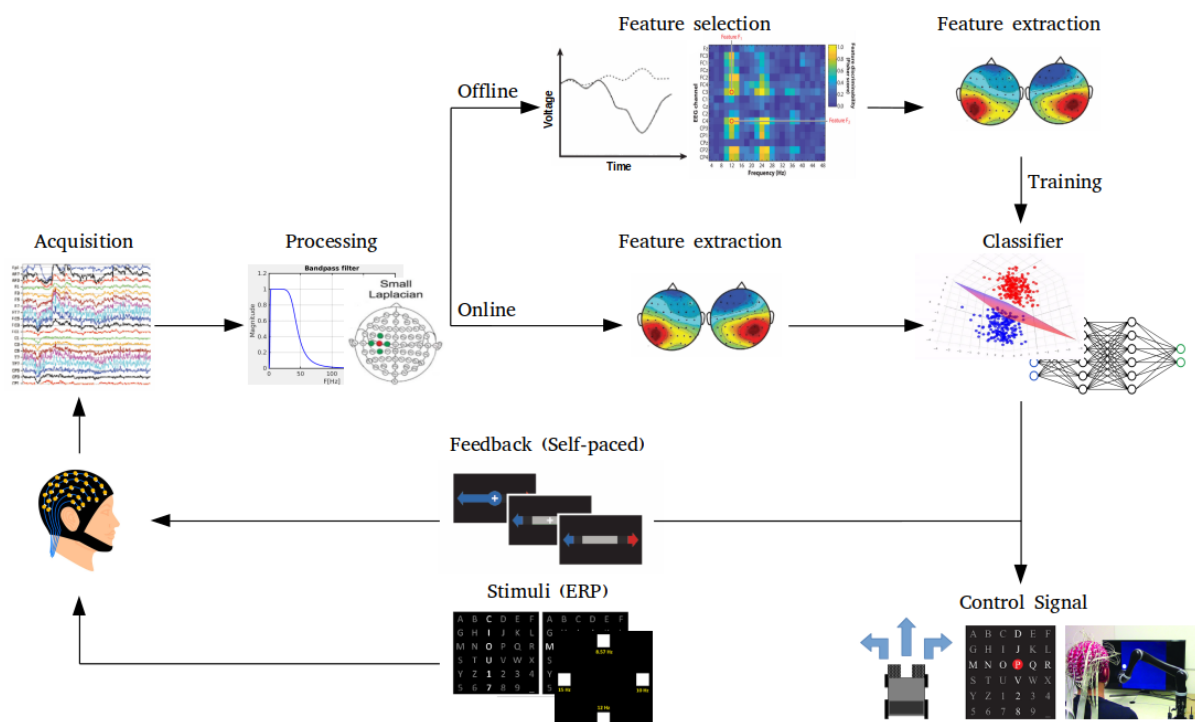


Figure 1.6: Scheme of the BCI loop. Two different phases can be distinguished: the Offline and the Online phase. During the Offline phase, the classifier is built based on the most discriminant features. The classifier is then used in the Online phase for delivering the control signals. In case of self-paced BCI, the loop is closed via a proper feedback.

1.3.2 Event Related Potential BCI

Event Related Potential are transient brain activities triggered by specific external stimuli, appearing as a finite series of waves named after their latency. They are characterized by a much lower amplitude compared to the continuous EEG signal. In order to extract them, averaging algorithms are applied to repeated epochs of the signal. Depending on the nature of the stimulus, they are classified as visual, cognitive, motor, or auditory [10]. Therefore ERP based BCIs exploit external stimuli in order to modulate the brain activity and parse the retrieved information into control signals.

P300

P300 signal is one of the most studied event related signal, it is part of the cognitive type, indeed it is elicited after a rare stimulus of interest is delivered to the subject. It appears as slow positive deflection after about 300ms the stimulus on set and it is usually predominant over the central parietal area [4]. Several experiments have shown the P300 potentiality in BCI, for example the P300 speller. In this particular application, for each trial the subject is presented a grid of letter of which each row and column correspond to a signal. The signal can be auditory, namely a different tone for each row and column, or visual, when rows and columns are lighted up randomly. The letter is selected as the match between the row and the column that elicited the P300 potential [4]. In order to identify the signal, time base feature, such as amplitude and wave shape, are used. Therefore the average between several trials is needed for extrapolating a clear and stable signal. For this reason the P300 speller was born as an extremely slow but reliable approach providing a letter every 26s with 95% of accuracy [4]. Although further studies tried to improve the information per time ratio, this still the biggest downside of the P300 speller approach [4]. The auditory ERP speller example is provided in Figure 1.7.

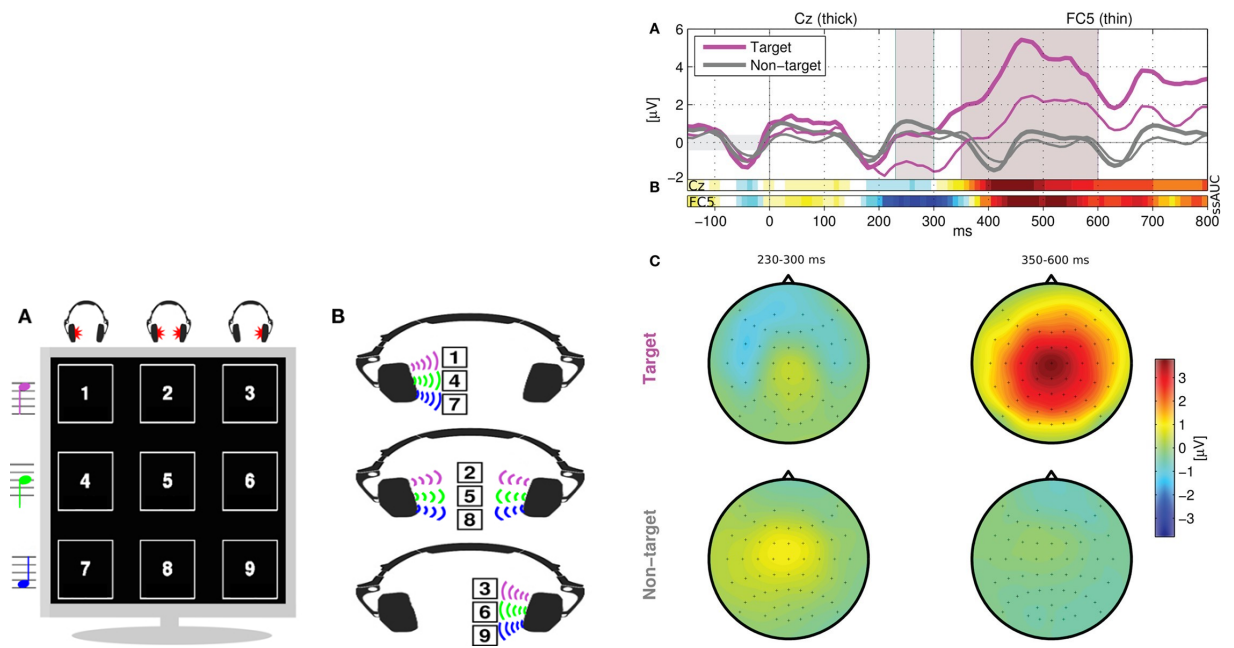
Steady State Visual Evoked Potential (SSVEP)

Steady State Visual Evoked Potential (SSVEP) represent an other valuable signal for BCIs. It consist on a resonance phenomenon elicited mainly over the visual cortex, in the occipital lobe, during the fixation of flickering light sources. In particular the SSVEP shows periodic properties that reflect the blinking frequency of the light stimulus. Thanks to frequency domain analysis, such as the power spectrum, it is possible to identify which is the presented stimulus and parse it in control signals [15]. Indeed, few experiment have been conducted aiming to drive a wheelchair exploiting SSVEP. During the trial the subject was asked to focus on a screen in which four squares were constantly flickering at 37 Hz (top), 38 Hz (right), 39 Hz (bottom) and 40 Hz (left). High frequencies have been used since they don't interfere with the spontaneous EEG and result more comfortable for the pilot. Power spectral density analysis

was then applied to the occipital EEG in order to retrieve the amplitude of the peaks in 37 Hz, 38 Hz, 39 Hz and 40 Hz. When a certain frequency showed the higher peak for more than 2s, the corresponding command was delivered to the wheelchair. An example of result is shown in Figure 1.8. Although the subject fatigue played an important role in decreasing the performances, this method allowed the user to reach the effective control even without a proper training [15].

Error-related Potential (ErrP)

Error-related Potential (ErrP) is an other evoked potential worth to mention. It is elicited after the subject recognizes an error and it is believed to have origin in the Anterior Cingulate Cortex (ACC), which is highly involved in the regulation of emotional responses. Three main type of ErrP have been distinguished depending on the source of the error, namely, response, feedback and observation ErrP [16]. The error ErrP is elicited after the subject realizes that it is performing the wrong task, for example a wrong movement. The feedback ErrP, instead, arises when the subject is notified that the choice it made is incorrect. Lastly, the observation ErrP occurs when the subject recognize that the action performed by a third operator is erratic [16]. While the first type is characterized by a large positive peak occurring between 200ms and 500ms, the other two types show a negative deflection taking place after 250ms [16]. Compared to the Error potential, the ErrP is a slow signal and it is suitable for a single trial detection exploiting low-pass filtering [16]. It has been shown as the ErrP may be implied as control gate in online BCI applications. In particular, if the ErrP is detected after presenting virtual feedback to the subject, the trial is rejected and no actual control signal is generated. This particular type of ErrP is called interaction ErrP [16]. A representation is provided in Figure 1.9. Further researches demonstrate how the ErrP can be involved in reinforcement learning paradigm in order to teach a robotic arm the optimal motor behavior to reach a target. In this case, the human cognitive capacities are used as a controller in the reinforcement learning loop, Figure 1.10, letting the robot understand which the target is and how to reach it [17].



(a) (A) 3×3 speller matrix design. (B) Distribution of the nine stimuli tones to the stereo channel of the headphone. T9 standard system is then used to help in selecting the right character [18].

(b) (A) Grand averaged ERPs at electrodes Cz (thick lines) and FC5 (thin lines). The ssAUC bars (B) quantify the discriminative information for the two channels. The averaged ERP scalp maps of target and non-target stimuli for the two marked time frames are shown in (C) [18].

Figure 1.7: Sound based P300 speller able to reach the speed of 0.89characters/min with an accuracy up to 92.63% for short sentences [18].

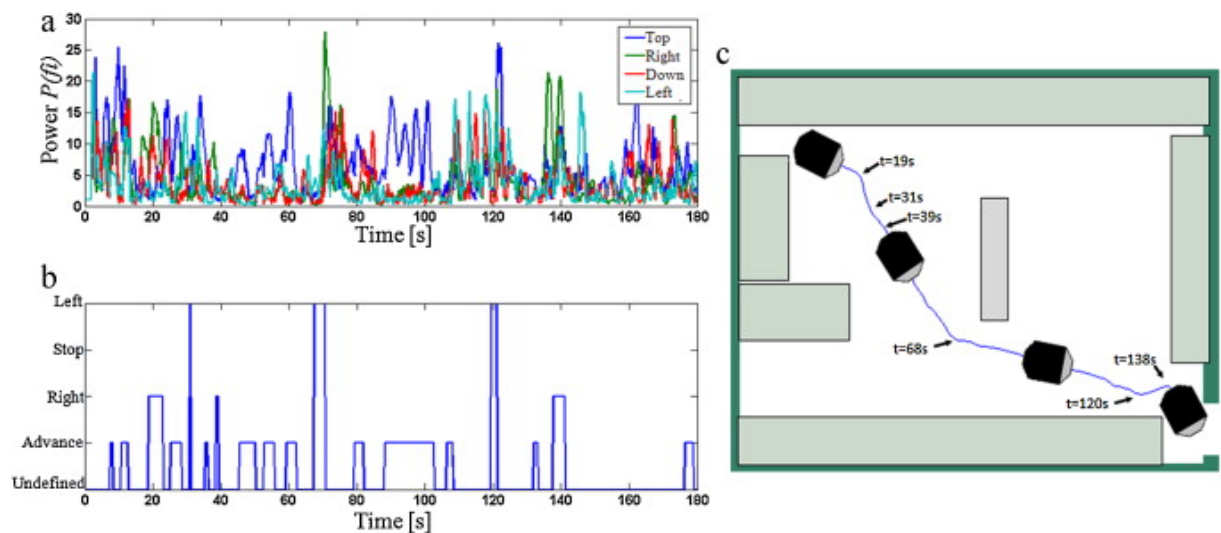


Figure 1.8: Driving test results of a SSVEP driven wheelchair. (a) SSVEP power spectrum over time; (b) Commands sent to the wheelchair based on the SSVEP powers showed in (a); (c) Path described by the wheelchair with time stamps corresponding to (b) [15].

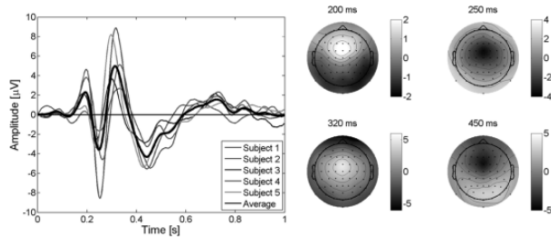


Figure 1.9: Interaction ErrP for 5 different subject at channel “FCz”, plus the grand average, with an error rate of 20%. Feedback is delivered at time 0 s. Scalp potential topographies, for the grand average EEG of the five subjects, at the occurrence of the peaks [16].

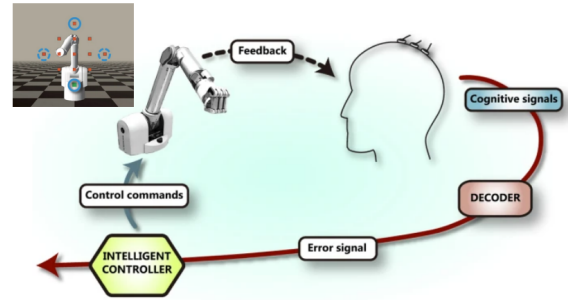


Figure 1.10: Reinforcement learning loop in which the human plays the role of controller through out the ErrP [17].

1.3.3 Self-paced BCI

The BCI techniques introduced so far rely on decoding the subject response after presenting particular external stimuli, meaning the produced cerebral signals merely reflect what is happening around the subject. In contrast, self-paced BCI systems are based on endogenous stimuli, namely signals that the subject voluntarily generates [9]. As already highlighted, a proper feedback system is therefore needed to help the subject understand the ongoing process and, if necessary, make corrections [3].

Covert Visuospatial Attention (CVSA)

During the last few years, Covert Visuospatial Attention (CVSA) signal has attracted the interest of several research groups as an alternative paradigm for self-paced BCI. CVSA is related to the process of focusing attention on different part of the visual field without the actual eye movement. It results in a lateralized modulation of the α band power over the parietal and occipital lobes, which reflect the endogenous shift of the attention target [19]. In particular, the power in the α band increases ipsilateral to the hemi-field containing the target the subject is focusing on, resulting in a topographical distribution over the lateral and posterior cortex [20]. An example of different activation across the cortex is provided in Figure 1.11. The feasibility of online BCI systems based on CVSA has been demonstrated for the first time by Tonin et al. group, that exploited a time-dependent approach in order to classify two classes, namely, bottom-left versus bottom-right [19]. In particular, the EEG signal acquired from the parieto-occipital regions was filtered in order to obtain sub-bands in the α range. Referring to the trial design (Figure 1.11), the period after 3000ms from the cue on set was divided into 150ms windows, and for each window a quadratic discriminant analysis classifier was built over the most discriminant features. The evidence for each window were accumulated thanks to a Bayesian

framework in order to deliver the classification at the end of the trial [19]. This paradigm was tested on 8 healthy subject, showing promising performances. Indeed none of the subject scored a results below the chance level, and the average accuracy across subjects reached $70.6 \pm 1.5\%$. Despite these preliminary results, additional studies that also involved the attempt to build a neurofeedback training for goalkeepers, revealed that CVSA-based BCIs are still in the early stages of development, and further research is needed to fully employ this method in real-world applications [21].

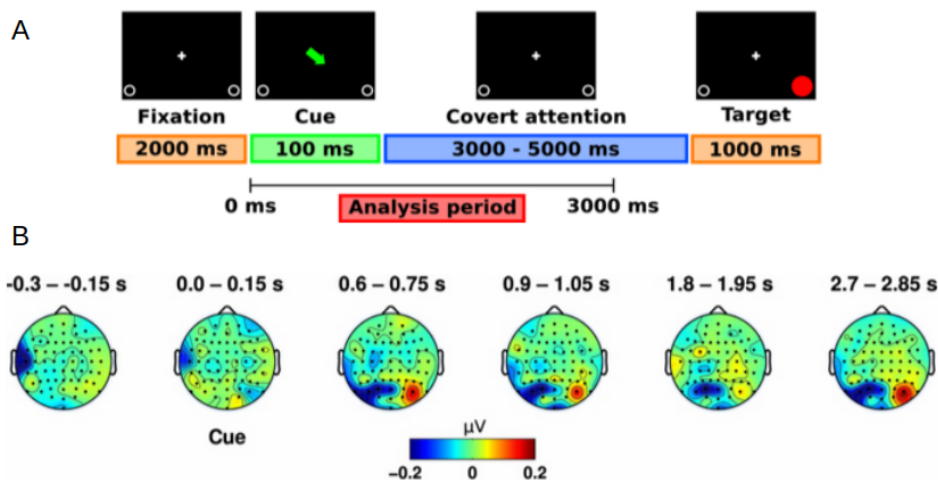


Figure 1.11: (A) Schematic trial representation for a CSVA task. The subject was asked to focus on the very bottom-right corner of the screen while staring at the cross located in the center of the screen. (B) Evolution of the envelope of the signals in the α band (8–14 Hz) over the EEG electrodes P7–8, PO7–8, O1–2. The topographic maps represent the difference between two attention conditions, namely right against left, in six different time windows. The signals were averaged across the ten healthy subjects that participated to the experiment [20].

Motor Imagery (MI)

Motor Imagery (MI) mental task is the most studied paradigm that lead to self paced signals. In particular the subject is asked to think about performing a certain movement without physically executing it, causing a modulation of the EEG activity highly localized both in frequency and in space domain [3]. Indeed, it has been shown that voluntary movements are preceded by the so called Event Related Desynchronization (ERD), which is a decrease of power in μ (8-12 Hz) and β (16-30 Hz) bands taking place 1.5s before the actual movement [22][23]. Furthermore, after the movement, an increase of power is recorded in the same frequency bands, producing the signal known as Event Related Synchronization (ERS) [23]. It is believed that ERD and ERS are phenomenon reflecting the recruitment of cortical neurons populations while performing a specific motor task [3]. In particular, ERD is given by the asynchronous activity of cortical neurons that are recruited in order to perform the task, and therefore a low amplitude and high frequency signal is recorded. Contrary, ERS occurs when the neurons activity is

synchronized, namely during the idling state that follows the task execution [22]. According to fMRI studies, compared to the movement task, MI task lead to the activation of similar and broader areas over the sensorimotor cortex [24]. Indeed ERD and ERS can be seen even without performing the actual movement [25]. Although the exact localization in space and frequency domain is subject specific, each task is characterized by specific localization according to the sensorimotor representation shown in Figure 1.12 [3]. For example, right or left hand MI would result in contralateral activity, namely around electrodes C1–3 and C2–4, respectively; while feet movement MI would be localized in the medial regions, namely around electrode Cz [3]. In Figure 1.13 is provided an example of ERD/ERS recorded both from a right hand movement task and a right hand MI task, showing similar behavior. In this example ERD/ERS were extracted through out the following steps: first the raw EEG signal was divided into event related trials, then for all the trials band-pass filters were applied in order to isolate the wanted frequency, the squared amplitude was then obtain and averaging across all trial was applied, lastly a smoothing filter was applied to reduce variability in the signal [22]. After the identification of a reference period (R) and an active period (A) along the trial, it was possible to quantify the ERD% as $ERD\% = 100 \times \frac{(A-R)}{R}$ [22]. An other example is provided in Figure 1.14, showing the difference in the activation due to left hand and right hand MI task over C3 and C4 EEG electrodes [25]. In conclusion, since different tasks lead to different activation of the cortex, Motor Imagery signals can be exploited for reliable BCI implementations exploiting proper trial designs as the one shown in Figure 1.15.

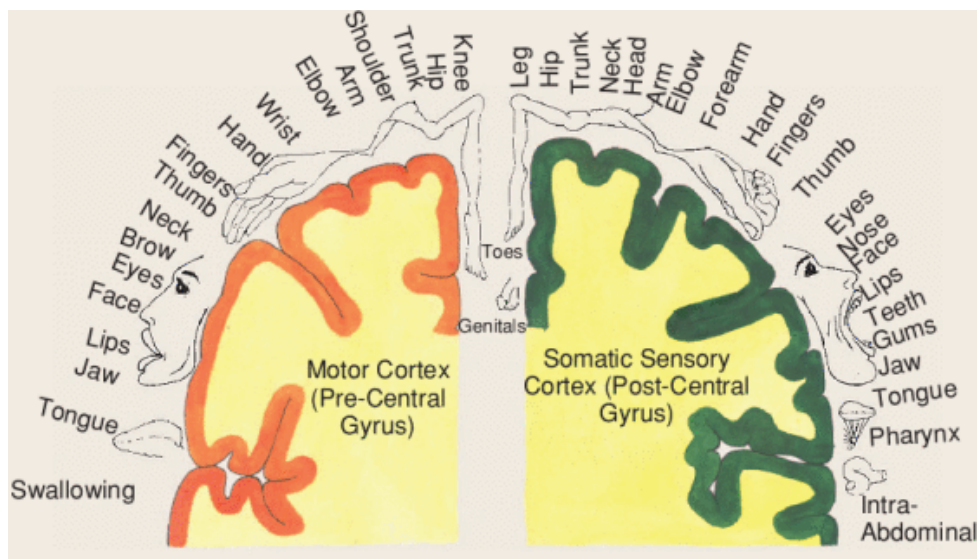


Figure 1.12: Sensorimotor representation on the motor cortex [12]

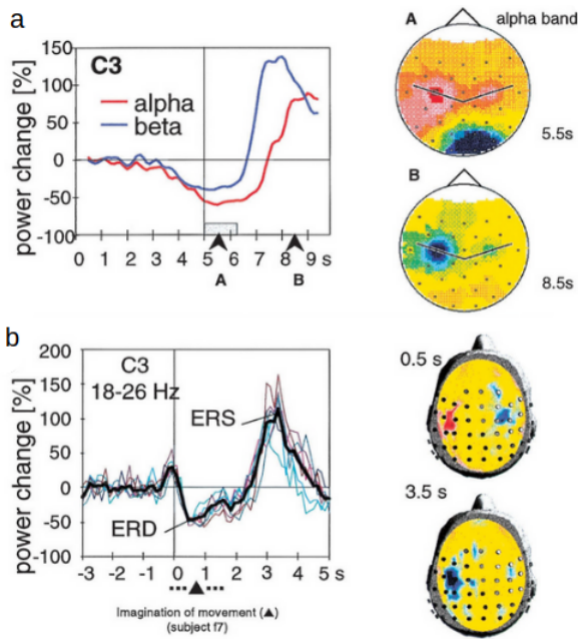


Figure 1.13: (a) Grand average ($n=9$) ERD curves calculated in the α and β bands in a right hand movement task. Grand average maps calculated for a 125ms interval during movement (A) and after movement-offset in the recovery period (B). (b) Superimposed ERD curves with β rebound from eight sessions with right motor imagery in one subject. C3 EEG channel in 18-26 Hz band is provided. ERD maps from one session displaying simultaneous contralateral ERD and ipsilateral ERS during and contralateral ERS after motor imagery. Areas are marked as ‘Red’ indicating ERD, and ‘blue’ for ERS [22].

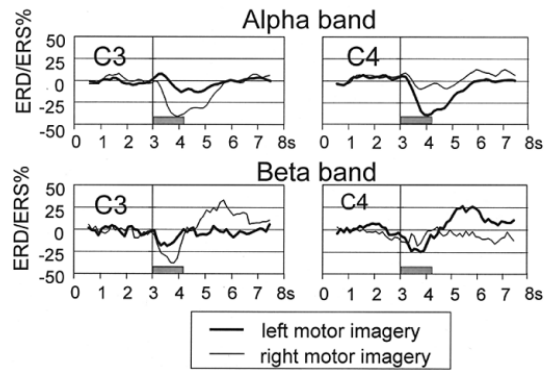


Figure 1.14: Grand average ERD/ERS curves recorded over left and right sensorimotor cortex during left and right hand motor imagery task. The ERD/ERS time courses were calculated for the α (upper panels, $n=16$) and β range (lower panel, $n=8$). Contralateral activation (ERD) is clearly visible. A gray bar indicates the time period in which the subject were asked to perform the mental task [25].

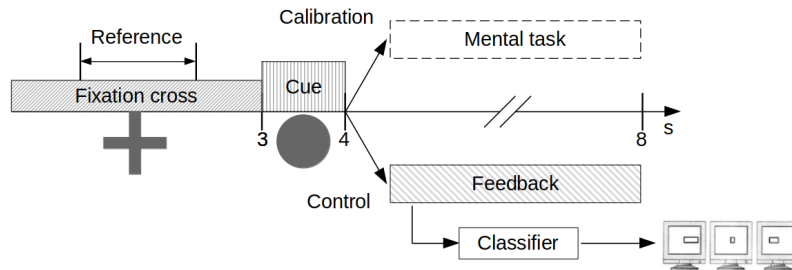


Figure 1.15: Graz imagination paradigm for MI based BCI [25]. First, the subject focuses on a cross displayed on the screen without performing any task. This period is also considered the reference period for further computations. Next, a cue symbol is presented, indicating which class the subject should perform in the following phase. During the control phase, active feedback is provided to the subject, reflecting the real-time output of the classifier.

Several studies have demonstrated the great potential of Motor Imagery based BCIs to improve the lives of patients suffering from various pathologies by enabling the control of robotic and prosthetic devices. For instance, Edelman et al. presented a BCI implementation to control a robotic arm through MI, highlighting the importance of using an effective learning paradigm to master the continuous control of the robotic device. [26]. In particular, the subjects used mental imagery of left versus right hand movements (left-right MI) and both hands versus rest (up-down MI) to directly control the horizontal and vertical movements of a cursor, in the first phase of the experiment, and subsequently, a real robotic arm. In order to train the subject, the novel continuous pursuit task, instead of using discrete trial tasks, was employed. Namely, the users had to continuously track a randomly moving target in a 2D workspace, requiring constant focus and motor imagery. This approach significantly increased user engagement and learning effectiveness compared to traditional tasks. Regarding the signal acquisition, EEG Source Imaging technique was used with the aim to improve the spatial resolution of the neural signals and reconstruct cortical activity. In order to distinguish the different tasks, frequency based feature were extracted particularly around the α band (8–13 Hz) power from motor-related electrodes, like C3 and C4. Finally, a stepwise linear regression based classifier was employed to optimize the electrode weights for task separation and provide real-time control. During all the process, users were provided with immediate visual feedback, reflecting the real-time output of the neural decoding algorithm [26]. The set up of the experiment and the feature extracted are provided in Figure 1.16.

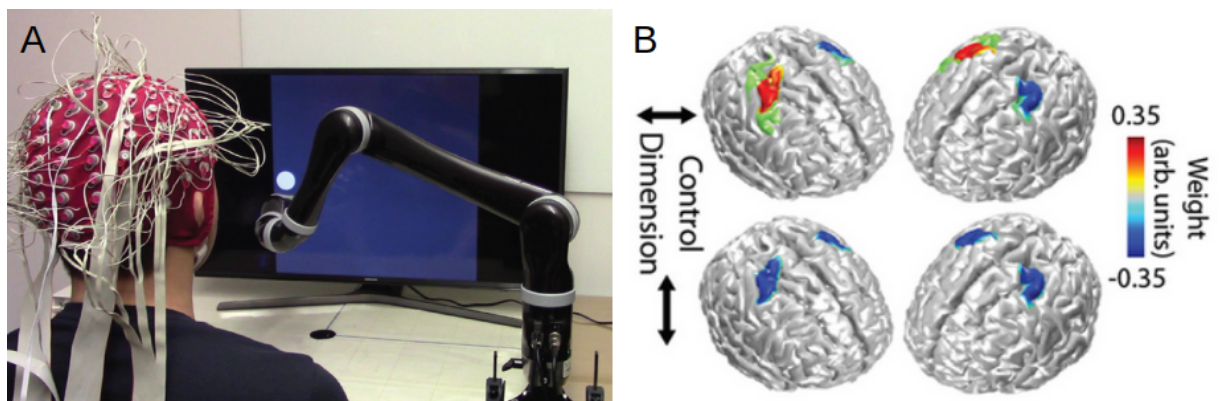


Figure 1.16: (A) Robotic arm continuous pursuit BCI setup. Users controlled the 2D continuous movement of a 7-degree of freedom robotic arm to track a randomly moving target on a computer screen. (B) Group-level feature maps for the horizontal (top row) and vertical (bottom row) control dimensions projected onto a template brain [26].

Although Motor Imagery based BCI can guarantee the direct control of robotic devices with high reliability in controlled environment, due to the limited numbers of commands that such a method is able to generate, the control of complex devices in a real-life situation remain challeng-

ing [3]. In order to overcome this limit, the research is heading toward the integration of human intention with the robot intelligence, leading to a shared semi-autonomous control. Tonin et al. explored this field presenting a preliminary study on the effects of the shared intelligence on the mental control of a telepresence robot [27]. In particular, the study involved two subjects with motor disabilities and four healthy subjects, all of them have been previously trained with the BCI. The subjects were asked to perform two motor imagery tasks, such as both feet versus both hand or left hand versus right hand, and each task was associated to a steering command (left or right), in addition the robot was set to go forward when no mental task was performed. EEG was recorded with a portable 16-channel g.tec device, with a sampling rate of 512Hz, and preliminary processing was applied to the raw signal. The processing involved the filtering through a band-pass filter between 0.1Hz and 100Hz, the application of a Laplacian spatial filter, and finally the computation of the Power Spectral Density (PSD) between 4Hz and 48Hz with a resolution of 2Hz over the last second, delivering 16 samples per second. For each sample, only the most discriminant features were fed to the statistical Gaussian classifier employed in this experiment. Furthermore, an exponential framework was used in order to stabilize the classifier output and accumulate evidence about the subject intention before delivering the actual command [27]. The telepresence robot, namely a three wheels powered Robotino, was equipped with nine infrared sensors able to detect nearby obstacles and a camera for telepresence purposes. A dynamical control system based on attractors and repellers was implemented in order to control the robot via BCI. Namely, when a command was delivered, the robot autonomously pursued the new target avoiding the obstacles [27]. The experiment showed how the shared control system allowed the subject to drive the robot along designed paths reducing the mental work load and improving the effectiveness of the delivered commands [27]. The same research group, Tonin et al., further proved the effectiveness of the shared control in a longitudinal study, which also remarked the concept of "mutual learning". This highlighted that not only the machine has to be trained on the subject, but subject also has to undergo proper training in order to develop strong and stable MI features [5]. The study followed the training of three tetraplegic subjects along a period of five, three and two months respectively, during which the subjects learnt to perform two motor imagery tasks, namely, imagine the movements of both hands and both feet. Their gained abilities were tested by driving a customized powered wheelchair, equipped with several sensors useful for the environment understanding, in a real scenario [5]. Details about the experiment are shown in Figure 1.17. Acquisition technique and classification method employed in this study were similar to the previous example [5]. At the end of the followup promising results have been recorded. In particular the shared control significantly improved the accuracy in hitting the target along the path from an average of $45.8 \pm 33.7\%$, without the assistance, to $72.5 \pm 32.5\%$, with the shared control [5]. Furthermore, the mutual learning paradigm helped the subjects increasing their performances along the time, as it is shown in Figure 1.18.

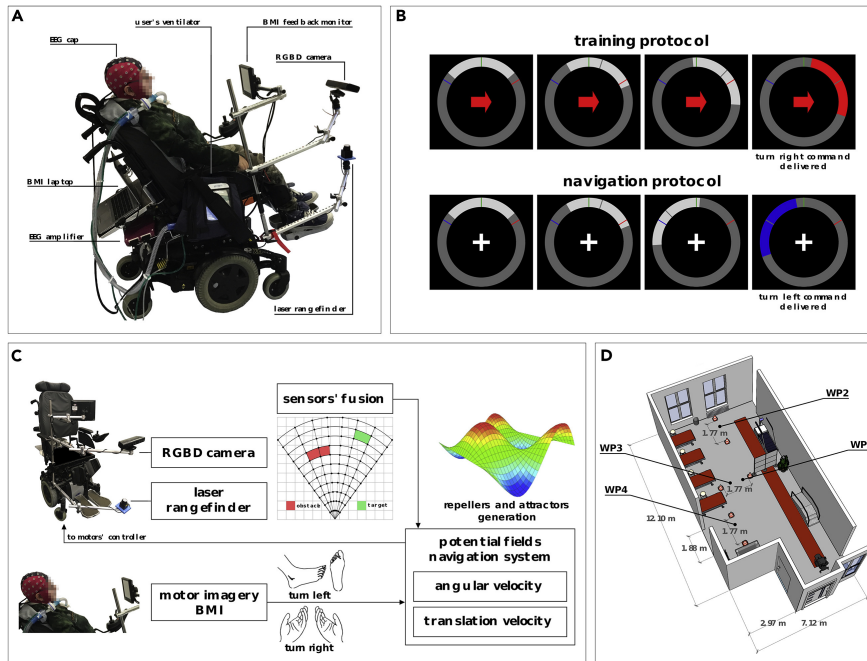


Figure 1.17: Experimental design and materials used in [5]. (A) Customized powered wheelchair equipped with an RGB-D camera, a laser rangefinder and a small monitor for the BCI feedback. (B) Two examples of the visual feedback presented to participants. In the upper row, the cued paradigm used during the calibration and evaluation sessions is illustrated. In the bottom, the feedback used during the navigation sessions, completely self-paced, without any cue, is shown. (C) Schematic representation of the shared-control navigation system. (D) Experimental field for the navigation phase of the study, in which participants were asked to mentally drive the wheelchair through four waypoints (WP1-4).

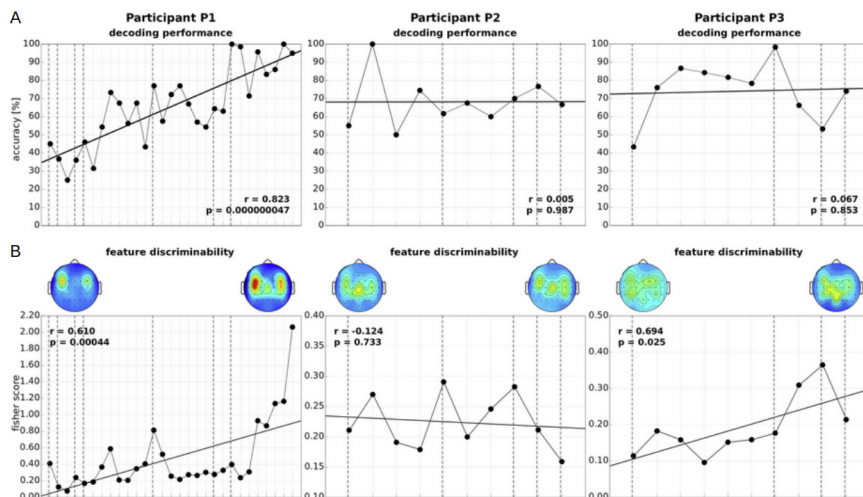


Figure 1.18: Mutual learning results retrieved from the study [5]. (A) Decoding accuracy over sessions for each participant. (B) Evolution of feature discriminability over sessions for each participant. On top, the topographic representation of the feature discriminability averaged over the first and the last 10 runs. In both (A) and (B) the solid black line represents the least-squares fit of the values, while the dotted line indicates when the decoder has been re-calibrated.

1.4 Thesis Objectives

In this thesis a novel technique has been explored with the aim of developing a semi-autonomous control system based on Motor Imagery BCI for driving a electrical wheelchair. In particular, the already existing BCI system developed by Tonin et al. [5] has been integrated with a Hidden Markov Model (HMM) to achieve two main goals. First, to interpret the binary Gaussian classifier output to retrieve an additional 'Rest' class, alongside the existing 'Both Hands' and 'Both Feet' motor imagery classes. Second, under the hypothesis that the probability of performing one task depends on the surrounding, the system incorporate environment information in the form of transition probability between classes, prior to the actual classification. A scheme of the project is provided in Figure 1.19, while the detail description of all the steps involved in this work is exposed in the following Methods chapter.

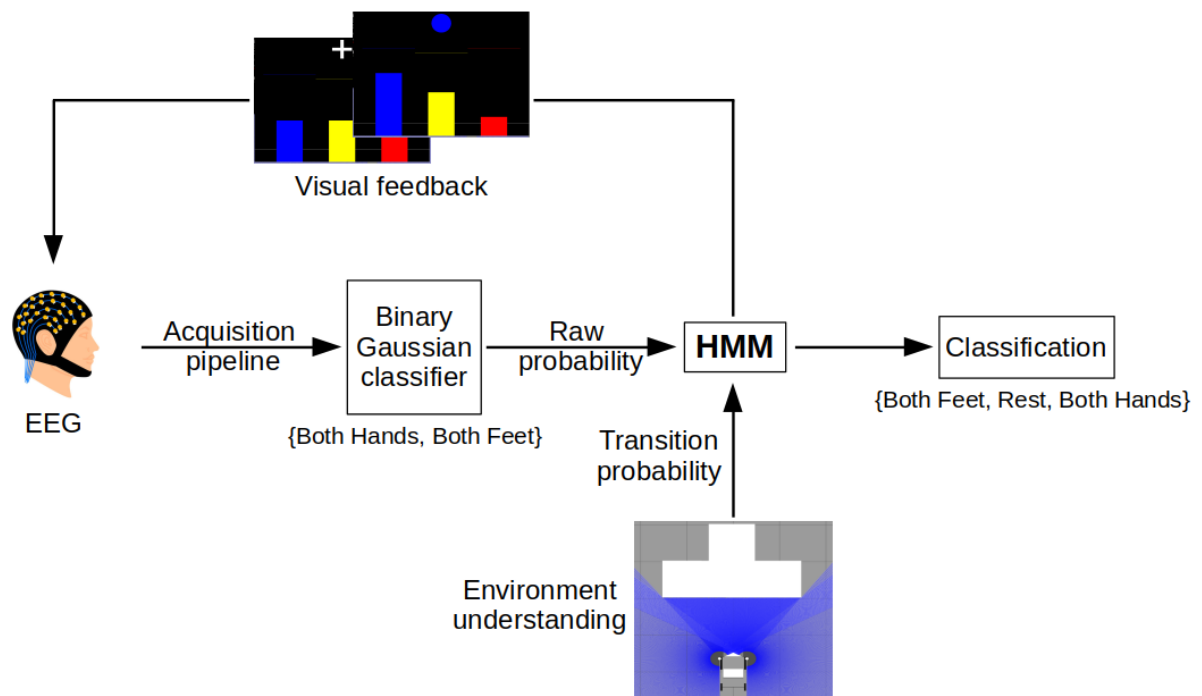


Figure 1.19: Illustration of the general purposes of the thesis.

2 Methods

This project has been realized exploiting ROS-Neuro, namely, a common open-source framework for BCI and robotics research and applications that relies on Robotic Operative System (ROS) [28]. The latter is considered to be the standard middleware in robotic application field, offering modularity and reliable communication infrastructure between different environments. Indeed, ROS-Neuro facilitates the interconnection between the different devices and processing steps that characterize a BCI system, offering software frameworks that boost their mutual integration [28]. Using the several nodes already implemented in ROS-Neuro, it was possible to build a BCI closed loop, like the one shown in Figure 1.6 page 13, and test the application.

2.1 Acquisition and Processing of EEG Data

EEG signal was acquired using the g.USBamp 16-channel amplifier setup by g.tec medical engineering, Edlinger, Austria. The g.GAMMAbox was used as driver for the 16 g.Ladybird active electrodes mounted on a g.GAMMAcap over the sensorimotor cortex according to the 10-10 system, namely, Fz, FC3, FC1, FCz, FC2, FC4, C3, C1, Cz, C2, C4, CP3, CP1, CPz, CP2, CP4. An additional ground electrode (GND) was placed on the forehead and a clip shaped reference electrode (REF) was ensured on the subject's ear lobe. All the electrodes were realized in sintered Ag/AgCl electrode material, with frequency range from 0 to 10 kHz, and needed the application of specific conductive gel (g.GAMMAgel) for a proper functioning. Figure 2.1 shows the acquisition devices, while the electrode map is provided in Figure 2.2a. The signal was acquired using the *rosneuro_acquisition* node and at the same time it was recorded in *.gdf* format by means of the *rosneuro_recorder* node. The General Data Format (GDF) is a standard for storing biomedical signals, allowing the file to be fully descriptive and specified [29]. In fact, information about the signal processing, duration, timing, and types of events presented during the acquisitions, along with other useful metadata, were saved alongside the raw signal in such files.

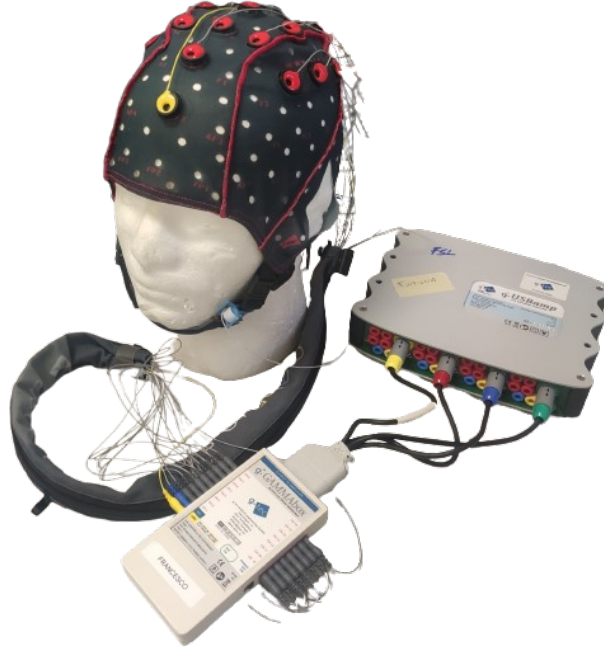
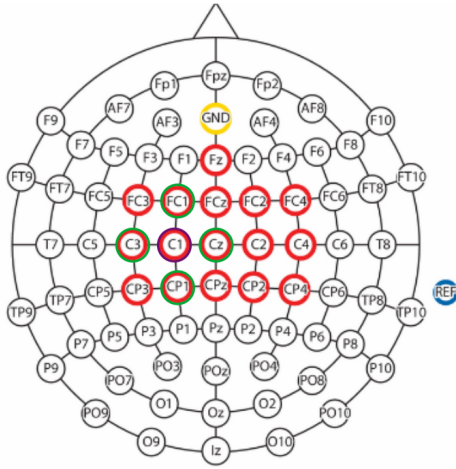


Figure 2.1: g.GAMMAcap with the 16 electrodes mounted over the sensorimotor cortex, connected to the g.GAMMAbox and the g.USBamp amplifier.

Exploiting the *rosneuro_processing* node, the raw EEG signal was spatially filtered with a Laplacian derivation in order to reduce the effect of volume conduction and enhance the spatial resolution [30]. Indeed the Laplacian filter acts as a high-pass filter, and is useful for highlighting differences in activation between adjacent electrodes [12]. The Laplacian filter was computed according to the formula 2.1, in which V_i^{lap} is the filtered signal from the channel i , V_i^{raw} is the original signal from the channel i , S_i is the set of the j electrodes surrounding the electrode i , and d_{ij} is the distance between electrodes i and j [30]. Laplacian filter was applied through out the row to column multiplication of each sample of raw data, coming from the 16 channel, to a 16x16 matrix (Figure 2.2b). Each column of such matrix is referred to a specific channel, in particular, the diagonal is filled with ones, while the extradiagonal cells are filled with the related weight, $-g_{ij}$, of all the other channels. In this case the distance d_{ij} is considered to be 1, since the electrodes in the S_i set are the adjacent ones, as shown in Figure 2.2a.

$$V_i^{lap} = V_i^{raw} - \sum_j (g_{ij} V_j^{raw}) \quad \text{where} \quad g_{ij} = \frac{\frac{1}{d_{ij}}}{\sum_{j \in S_i} (\frac{1}{d_{ij}})} \quad (2.1)$$



(a)

	Fz	FC3	FC1	FCz	FC2	FC4	C3	C1	Cz	C2	C4	CP3	CP1	CPz	CP2	CP4
Fz	1.00	0.00	0.00	-0.25	0.00	0.00	0.00	0.00	0.00	0.00	0.00	0.00	0.00	0.00	0.00	0.00
FC3	0.00	1.00	-0.33	0.00	0.00	0.00	-0.33	0.00	0.00	0.00	0.00	0.00	0.00	0.00	0.00	0.00
FC1	0.00	-0.50	1.00	-0.25	0.00	0.00	0.00	-0.25	0.00	0.00	0.00	0.00	0.00	0.00	0.00	0.00
FCz	-1.00	0.00	-0.33	1.00	-0.33	0.00	0.00	0.00	-0.25	0.00	0.00	0.00	0.00	0.00	0.00	0.00
FC2	0.00	0.00	0.00	-0.25	1.00	-0.50	0.00	0.00	0.00	-0.25	0.00	0.00	0.00	0.00	0.00	0.00
FC4	0.00	0.00	0.00	0.00	-0.33	1.00	0.00	0.00	0.00	0.00	-0.33	0.00	0.00	0.00	0.00	0.00
C3	0.00	-0.50	0.00	0.00	0.00	0.00	1.00	-0.25	0.00	0.00	0.00	-0.50	0.00	0.00	0.00	0.00
C1	0.00	0.00	-0.33	0.00	0.00	0.00	-0.33	1.00	-0.25	0.00	0.00	0.00	-0.33	0.00	0.00	0.00
Cz	0.00	0.00	0.00	-0.25	0.00	0.00	0.00	-0.25	1.00	-0.25	0.00	0.00	0.00	-0.33	0.00	0.00
C2	0.00	0.00	0.00	0.00	-0.33	0.00	0.00	0.00	-0.25	1.00	-0.33	0.00	0.00	0.00	-0.33	0.00
C4	0.00	0.00	0.00	0.00	0.00	-0.50	0.00	0.00	0.00	-0.25	1.00	0.00	0.00	0.00	0.00	-0.50
CP3	0.00	0.00	0.00	0.00	0.00	0.00	-0.33	0.00	0.00	0.00	0.00	1.00	-0.33	0.00	0.00	0.00
CP1	0.00	0.00	0.00	0.00	0.00	0.00	0.00	-0.25	0.00	0.00	0.00	-0.50	1.00	-0.33	0.00	0.00
CPz	0.00	0.00	0.00	0.00	0.00	0.00	0.00	0.00	-0.25	0.00	0.00	0.00	-0.33	1.00	-0.33	0.00
CP2	0.00	0.00	0.00	0.00	0.00	0.00	0.00	0.00	0.00	-0.25	0.00	0.00	0.00	-0.33	1.00	-0.50
CP4	0.00	0.00	0.00	0.00	0.00	0.00	0.00	0.00	0.00	0.00	-0.33	0.00	0.00	0.00	-0.33	1.00

(b)

Figure 2.2: (a) Electrode map used in the project. The electrode highlighted in red are the ones mounted on the cap. The electrode marked in green are the neighbors electrode for the electrode C1 according to the Laplacian filter. (b) 16x16 Laplacian filter matrix.

After the spatial filtering, thanks to the *rosneuro_processing* node, the Power Spectral Density (PSD) was computed for each channel in order to study how the different frequency bands changed during time. In theory, infinite time points are needed for computing the exact PSD, but since this is not possible in a real scenario, the Welch's algorithm was used to extract a PSD estimation [31]. Namely, a buffer of 512 samples (1 second) was divided into three subsequent windows of 256 sample (0.5 second) overlapped by 50%, each window was filtered with a Hamming window in order to reduce the frequency leakage effect, and then the Fast Fourier Transform (FFT) was computed for each of them [31]. Finally, the three FFTs obtained were averaged in order to reduce the variability in the estimated PSD, and the Logarithm transformation was applied to enhance the signal scale. The process was repeated for each shift of 32 samples (0.0625 seconds) of the main buffer. Thanks to this algorithm, the estimation of the channel wise PSD along the time was obtained with a resolution of 2Hz, resulting in a matrix $windows \times frequency \times channel$. Since Motor Imagery tasks elicit variation in α and β bands, only the frequencies between 2Hz and 48Hz were considered during the feature selection process. As a result of the PSD computation, the initial sample frequency of 512Hz was reduced to 16Hz. A scheme of the PSD computation process is provided in Figure 2.3

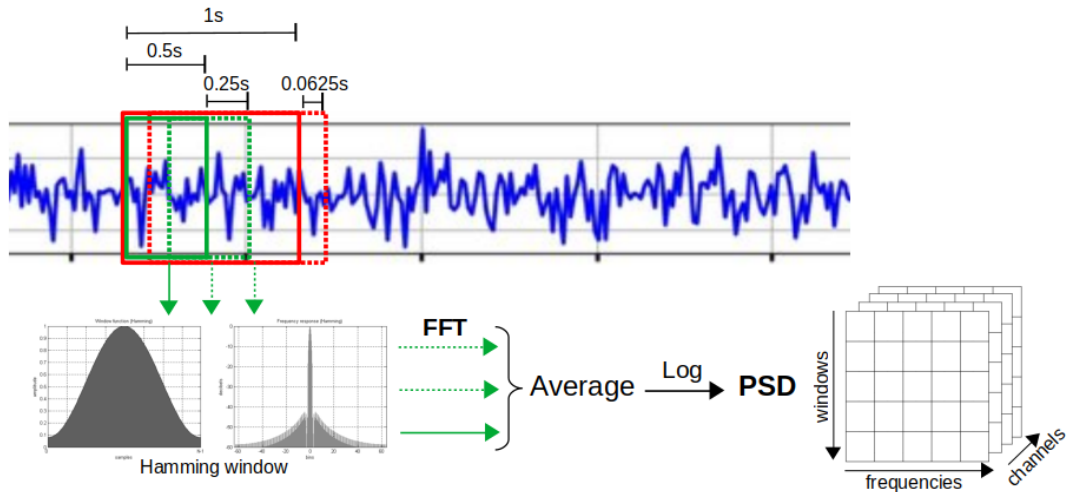


Figure 2.3: Scheme of the Welch's algorithm for the estimation of the PSD.

2.2 Calibration and Feature Selection

Subject specific features were retrieved from the Calibration runs in order to train the binary Gaussian classifier. During the calibration phase, a wheel animation (Figure 2.4) guided the subject through the trials. In particular, first a fixation cross was shown for 2 seconds in the center of the screen, then the cue ball appeared in the same place for 1 second indicating the task type the subject was asked to perform in the following period. More precisely, a blue ball was shown for the 'Both Feet' task, a red one for the 'Both Hands' task, and a yellow one for the 'Rest' task. After the cue period, the wheel animation started moving automatically for a random time between 4 seconds and 5.5 seconds, indicating the subject the time span to perform the task suggested by the cue. at the end of the active period, a 1 second pause was used to divide subsequent trials. Although it was not necessary for the classifier training, also the 'Rest' task was acquired for subsequent offline analysis. Multiple calibration runs were acquired, especially the first time, for assessing the subject's features strength and stability. Further details about the calibration runs are provided in the Result chapter.

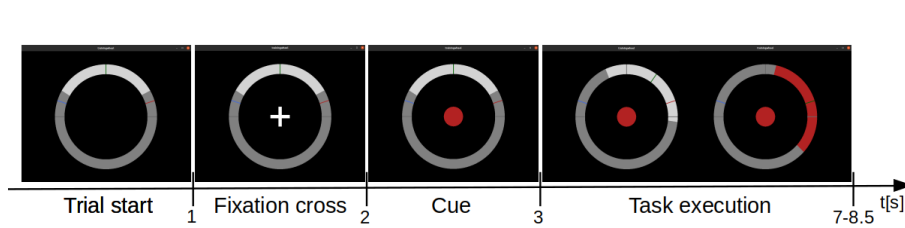


Figure 2.4: Calibration trial design based on the *rosneuro_feedback_wheel* package. The figure shows the sequence of events that characterized the several calibration runs. In this particular sequence the subject was asked to perform the 'Both Hands' task.

Once enough data were collected, a MATLAB tool was used to select the most discriminant features and train the classifier. The feature selection process relied on the Canonical Variate Analysis (CVA). CVA is a multivariate statistical technique that uses linear combination of the original features to create new features called canonical variates, that maximize the separation between the classes [32]. In particular, for each frequency retrieved with the PSD, given that s_{ij} is the sample ($1 \times channels(ch)$) at instant j for the class i , and k is the number of classes, and n_i is the number of sample for the class i , the sample matrix S can be built as shown in the formula 2.2.

$$S = \begin{bmatrix} S_1 \\ \vdots \\ S_i \\ \vdots \\ S_k \end{bmatrix}_{n \times k} \quad \text{where} \quad S_i = \begin{bmatrix} s_{i1} \\ \vdots \\ s_{ij} \\ \vdots \\ s_{in_i} \end{bmatrix}_{n_i \times ch} \quad (2.2)$$

Consequentially, the eigenvectors for the first $k-1$ non-zero eigenvalues λ of the matrix $W^{-1}B$ are computed. Formulas 2.3 and 2.4 show the computation of the within-classes dispersion matrix W and the between-classes dispersion matrix B , respectively [32].

$$W_{ch \times ch} = \sum_{i=1}^k \sum_{j=1}^{n_i} (s_{ij} - m_i)'(s_{ij} - m_i) \quad \text{where} \quad m_i = \frac{1}{n_i} \sum_{j=1}^{n_i} s_{ij} \quad (2.3)$$

$$B_{ch \times ch} = \sum_{i=1}^k n_i (m_i - m)'(m_i - m) \quad \text{where} \quad m = \frac{1}{n} \sum_{i=1}^k n_i m_i \quad (2.4)$$

The obtained $k-1$ eigenvectors, of dimension $ch \times 1$, are used to build the matrix $A_{ch \times k-1}$, thanks which is finally possible to retrieve the canonical variates as the projection 2.5 [32].

$$Y_{n \times k-1} = SA \quad (2.5)$$

Note that in this particular study the number of classes k is two, therefore only one eigenvector is selected for the projection into the canonical variates space. Once the canonical variates are computed, channels are ranked based on their Discriminant Power (DP), namely their contribution on the new feature space. The DP computation is based on the structure matrix T (formula 2.6), namely the correlation matrix between the original feature S and the canonical variates Y , and the normalized eigenvalues γ_u (formula 2.7).

$$T = corr(S, Y) \quad \text{whose element} \quad t_{eu} = corr(S_e, Y_u) = \frac{cov(S_e, Y_u)}{\sigma_{S_e} \sigma_{Y_u}} \quad (2.6)$$

$$\gamma_u = \frac{\lambda_u}{\sum_{u=1}^{k-1} \lambda_u} \quad (2.7)$$

Therefore, for each frequency and for each channel, the DPs are computed following the equation 2.8, building the so called discriminability map [32].

$$DP_e = 100 \times \frac{\sum_{u=1}^{k-1} \gamma_u t_{eu}^2}{\sum_{e=1}^{ch} \sum_{u=1}^{k-1} \gamma_u t_{eu}^2} \quad (2.8)$$

The discriminant analysis results are displayed in an ad hoc MATLAB GUI, which provides the discriminant power of features for each calibration run, highlighting the most stable features across different runs. The feature selection process is not entirely automated, as the GUI allows the user to manually select the most relevant features, also taking into account their physiological significance. Figure 2.5 displays the MATLAB GUI for better understanding.

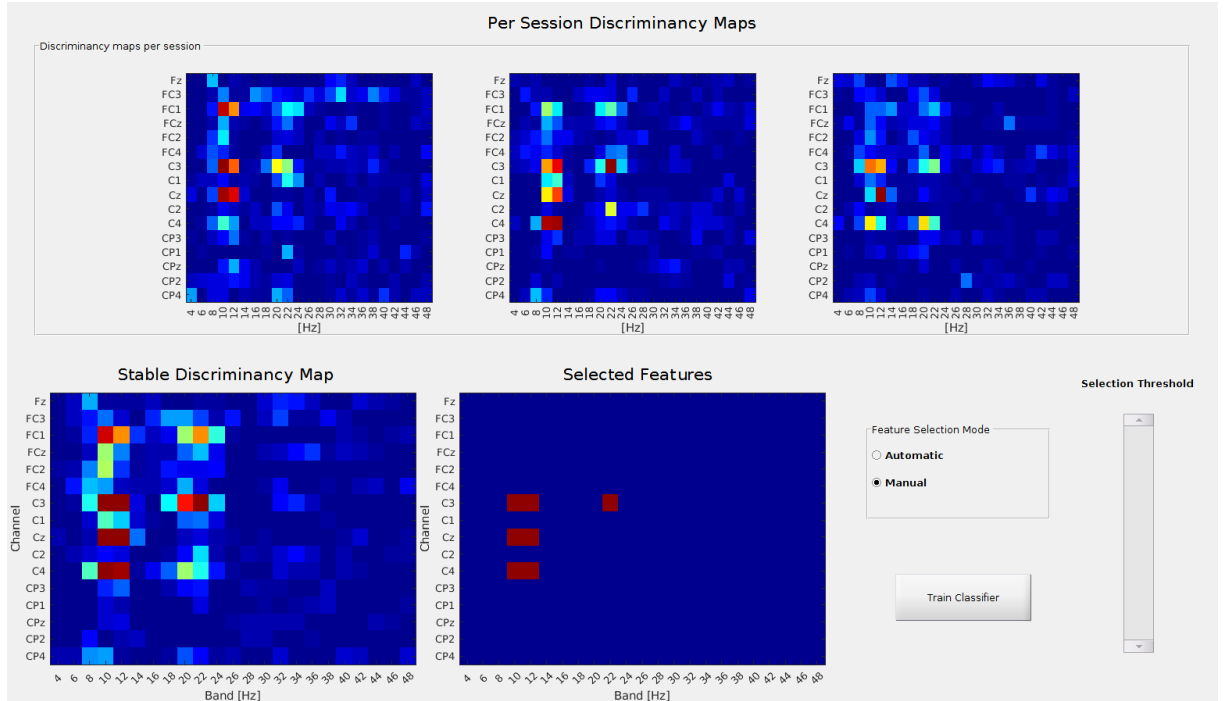


Figure 2.5: MATLAB GUI for feature selection showing an example of good features. In the top the discriminability map for each calibration run are provided, in this case three calibration runs were acquired for the tasks 'Both Hands' and 'Both Feet'. The average result is shown in the bottom left, while the selected feature are displayed in the bottom center. The bottom right selector allows to switch between the manual and the automatic selecting mode. The first one allows to manually select and deselect the wanted feature using the mouse pointer, while the second one automatically mark as relevant all the features above a certain discriminant level, which is adjustable through out the dedicated sliding cursor. The selected features are then used to train the Gaussian classifier as soon the *Train Classifier* button is pressed.

2.3 Binary Gaussian Classifier

After the feature selection process, the binary Gaussian classifier was trained over the distribution of the most discriminant features. In particular, the standard Maximization and Estimation (EM) algorithm, implemented in the same MATLAB tool, was used to retrieve the parameters for the $n_{classes}(2) \times n_{feature}$ Gaussian Mixture Model (GMM) that composed the classifier. Each GMM consisted in only one element, characterized by two parameters, namely the mean and the standard deviation, leading to a total of $n_{classes}(2) \times n_{feature} \times 2$ parameters. Once the classifier was trained, all the parameters and information were saved in a binary format (.dat) in order to be incorporated in the main pipeline, more precisely, in the *rosneuro_processing* node. Hence, during the Online (or Control) phase only the selected features were extracted from each PSD sample, and the likelihoods over the probability density function of each class were computed. The equation 2.9 shows how the sample's likelihood for each class was computed. In the formula x is the sample array $1 \times n_{features}$, while M_j and C_j are, respectively, the array of mean and variance for the $n_{features}$ GMM for the class j . The likelihoods were then normalized to determine the probability of the sample belonging to each class, resulting in an output vector of $1 \times n_{classes}$, namely 1×2 , for each sample. This probability was then fed to the Hidden Markov Model for further processing.

$$Likelihood_j = \frac{1}{\prod_{i=1}^{n_{classes}} (\sqrt{C_j})} e^{-\frac{1}{2} \sum_{i=1}^{n_{classes}} \frac{(x - M_j)^2}{C_j}} \quad (2.9)$$

2.4 Hidden Markov Model and Traversability

The raw probability output of the binary Gaussian classifier was interpreted by the Hidden Markov Model (HMM) in order to retrieve the three classes: 'Both Feet', 'Rest' and 'Both Hands'. During the process the surroundings information where also integrated prior the final classification. A brief introduction about the HMM can be found in the Appendix at page 50.

2.4.1 HMM Structure

In this project the HMM has been designed based on two main hypothesis. First, the EEG depends on the task the subject want to perform, thus the state can be described by the output of the Gaussian classifier. Second, the probability of performing one task depends also on the information about the surrounding. Therefore the HMM was characterized by the following properties:

- Each state represented a particular class. Therefore, the model consisted of 3 hidden

states, namely, 'Both Hands', 'Both Feet', and 'Rest'. For reference, the HMM scheme is provided in Figure 2.6.

- The probability of changing classes, namely the transition probability matrix $T(t)$, depended on the information about the surroundings, and therefore was time varying.
- The Observations consisted on the output of the binary Gaussian classifier. In particular the distribution of the probability that the sample belonged to one of the two classes ('Both Hands' and 'Both Feet') chosen as reference.

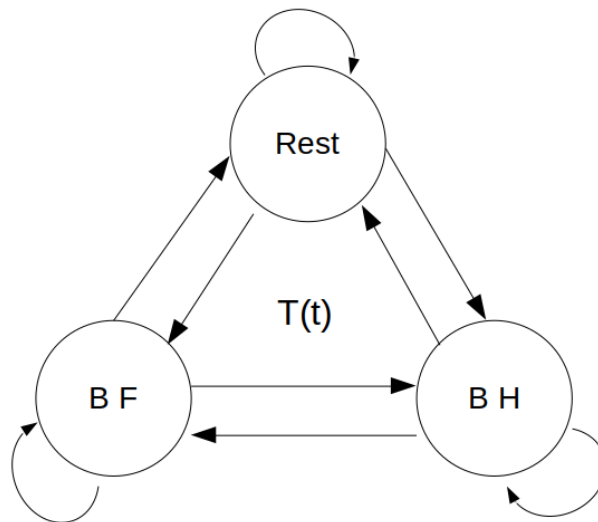


Figure 2.6: Scheme of the HMM used in this project. The model features three hidden state, one for each class. BF stands for 'Both Feet' and BH stands for 'Both Hands'. While the transition matrix $T(t)$ is time varying and depends on the surroundings.

2.4.2 HMM states

Each HMM state consisted on a Probability Distribution Function (PDF) designed after the expected distribution of the probability output of the binary classifier. In particular, based on the experiences acquired over more than ten years of usage of this Gaussian classifier, it has been noticed that when good discriminant features are selected, the probability distribution tends to be concentrated at the extremes, with values collapsing near the boundaries of 0 and 1 [33]. More in details, when the subject is performing an active task ('Both Hands' or 'Both Feet'), the probability output for that task is more likely to be near 1. Instead, while performing the 'Rest' task it is possible to notice a split on the probability distribution mostly concentrated around 0 and 1 [33]. More evidences about the real distribution and the erratic behavior of the classifier are provided and commented in the Results chapter at page 38. Thus, the ideal probability output corresponding to the reference class was considered in designing the PDFs

that characterize each HMM state. The following equations were used, where pp represents the raw probability output of the Gaussian classifier for the 'Both Feet' class.

- Both Feet: $10e^{20(pp-1)} + 5e^{8(pp-1)}$
- Both Hands: $10e^{-20pp} + 5e^{-8pp}$
- Rest: $(10e^{20(pp-1)} + 5e^{5(pp-1)} + 10e^{-20pp} + 5e^{-5pp})/2$

For better comprehension, Figure 2.7 shows the ideal distributions per class with the normalized PDF superimposed on each graph. While further discussion about the choice of the PDFs is provided in the Discussion chapter at page 47.

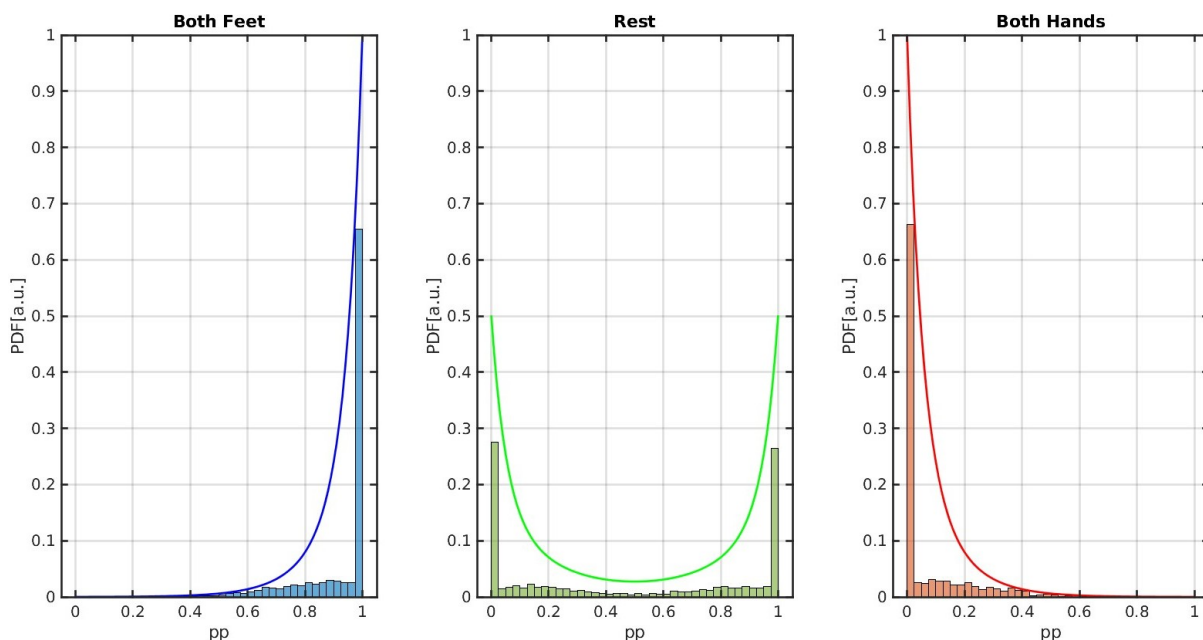


Figure 2.7: Each graph represent the histogram of the ideal raw output probability of the binary Gaussian classifier for the class 'Both Feet' over the three classes. The normalized PDF of the HMM state is superimposed on each respective graph.

2.4.3 Traversability and Transition Matrix

The surrounding information were incorporated into the model in the form of transition matrix $T(i)$. Indeed, after assigning direction to each task, such as 'Both Feet' for left, 'Rest' for forward, and 'Both Hands' for right, the transition matrix embedded the information about the probabilities to pass through each direction. In particular, the wheelchair was equipped with an RGB-D camera and lidar sensors as in the previous study [5]. The sensors signals were acquired and integrated into the system exploiting ROS, more in details the *move_base* package was employed to retrieve the *costmap_2d* matrix. This consists on a 200×200 matrix with a resolution

of 0.05m in which each cell is assigned with a score from 0 to 255 based on the risk of collision with the objects in the surrounding, where 0 stands for no risk and 255 stands for certain collision. Since the *costmap_2d* is always oriented along the xy axes, an *odometry* system was implemented to get the real orientation of the wheelchair and reinterpret the occupancy values. Starting from the *costmap_2d*, the 3×3 transition matrix for the HMM was retrieved through out the following steps. An explanatory illustration is provided in Figure 2.8.

- The *costmap_2d* matrix was divided into three angular sectors, considering the zero angle as aligned with the wheelchair orientation. As a result the left view $[30^\circ, 100^\circ]$, the front view $[30^\circ, -30^\circ]$, and the right view $[-30^\circ, -100^\circ]$ were retrieved.
- For each view the total occupancy was computed summing up all the values in the respective angular sector, forming the *occupancy array* (1×3). This array was then normalized in order to obtain the *occupancy probability* for each view.
- The *reverse occupancy* was computed starting from the *occupancy array* as shown in the equation 2.10. This array was then normalized obtaining the *reverse occupancy probability*.

$$\text{reverse occupancy} = \left| \text{occupancy array} - \sum \text{occupancy array} \right| \quad (2.10)$$

- The central row of the transition matrix, which expresses the probability to jump from the 'forward' state to another or the same state, was computed as the normalized array resulting from the equation 2.11. In this way, if a direction was strongly occupied *1-occupancy probability* was extremely low and further lower the *reverse occupancy probability*. Vice versa, if a direction was mostly free *1-occupancy probability* tent to 1 and did not modify the *reverse occupancy probability*.

$$\text{traversability} = (1 - \text{occupancy probability}) \times \text{reverse occupancy probability} \quad (2.11)$$

- The computation of the first and the third row of the transition matrix was based on the concept that if the subject is turning into a direction, which is free of obstacle, the most likely choice is to proceed in the same direction, namely to stay in the same state. Thus, starting from the *traversability* array the left and the right directions were incremented by 40% prior the normalization for the first row and the third row respectively.

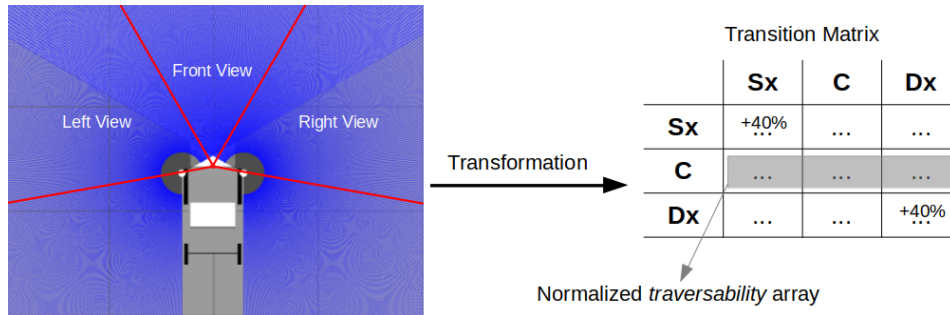


Figure 2.8: The wheelchair surrounding is first split into three sectors (on the right), following the mentioned steps was possible to retrieve the transition matrix (on the left). After applying the +40% the array is re-normalized in order to build the first and the third row of the transition matrix. Dx stands for right, C stand for forward, and Sx stands for left. Each direction was assigned to one of the three task, namely, 'Both Hands', 'Rest', and 'Both Feet'.

2.4.4 HMM Forward Step

Finally, the Forward algorithm, whose a theoretical introduction can be found in the Appendix, was used in order to access the probability of being in each state at time t given a series of observations and the current transition matrix. The observation consisted in a 1 second long (16 samples) FIFO (first input first output) buffer of raw probability output of the binary Gaussian classifier for the reference class 'Both Feet'. Also the transition matrix where computed with a frequency of 16Hz to be aligned with the sample frequency. Thus, every time the buffer was updated with a new sample, the forward step proceeded as follow. First, the buffer's overall likelihood was computed across the three classes PDFs. In particular, for each class, the likelihood of each sample was evaluated and the overall likelihood was computed as the product of the single sample likelihoods. The resulting 1×3 array was then normalized, obtaining the $likelihood(t)$ array. Consequently, the $posterior(t)$ was obtained as the normalized array resulting from the equation 2.12, in which the $posterior(t-1)$ is the 1×3 array of posterior probability computed in the previous step, and $T(t)$ is the 3×3 lastly updated transition matrix. During the first cycle, the $posterior(t-1)$ was considered to be equally probable across the states, as was $T(t)$ if it had not been updated yet.

$$absolute\ posterior(t) = likelihood(t) \times posterior(t-1) \cdot T(t) \quad (2.12)$$

2.5 Exponential Smoother

The HMM output was filtered with an exponential smoother based on the concept of the exponential framework used in previous studies [5][27][33]. The exponential smoother acted as

a low-pass filter on the probability value assigned to each class in order to accumulate evidences about the classification and stabilize the HMM output. In addition, thanks to this filter the changes on the class probability were slowed down, letting the visual feedback to be more comfortably controlled by the BCI user. The exponential smoother followed the equation 2.13, where α is the smoothing factor and express how much the previous value is considered in the computation of the new one. Higher is this parameter, larger is the instantaneous classification change needed to modify the output. In this project α where set to 0.96. Following the experimental design, the initial value of the probability were set to 0.33 every time a new trial started in order to start form an equally probable condition across the classes.

$$output(t) = \alpha \times output(t - 1) + (1 - \alpha) \times HMM(t) \quad (2.13)$$

2.6 Evaluation Protocol

In order to access the efficacy of the HMM implementation, the virtual environment of ROS-Gazebo was employed. In particular, a virtual model of the wheelchair, equipped with all the sensors for the environment understanding, was placed in an empty world in which random objects were spawned following a precise trial design. More precisely, the subject was guided by an ad hoc visual feedback through out the series of trial phases, namely: 1s rest phase at the beginning of each trial; 2s of fixation cross; 1s of cue, in which the subject was instructed on the task to perform on the following phase; the continuous feedback period with a variable duration between 4s and 5.5s, during which the subject was able to actively control the visual feedback, consisting on three vertical bars that represented the probability assigned to each class; lastly, 1s was employed to show the result of the trial. The trial was considered to be 'Hit' if the probability for the cue class reached the respective tunable threshold, contrary the trial was claimed to be 'Miss' if the time limit was reached or a wrong class reached the respective threshold. In addition, the sequence of task was random for a total of 10 trial per class for each evaluation run. The trial design and the visual feedback are provided in Figure 2.9 for better understanding. Three different types of evaluation were used: one with an equally probable transition matrix (T_{off}), one with spawning objects presenting only the cue task as open direction (T_1), and one with spawning obstacles leaving two open directions (T_2). Thus, different level of environment integration were tested to access the system effectiveness in helping the subject to perform the right task. Figure 2.10 provides the obstacle shape and the resulting transition matrix. During the evaluation runs, only the visual feedback was presented to the subject, who was not informed about the evaluation type in order to prevent influencing their control strategy. Furthermore, the three evaluation types were delivered randomly to the subject to ensure independence from fatigue factors.

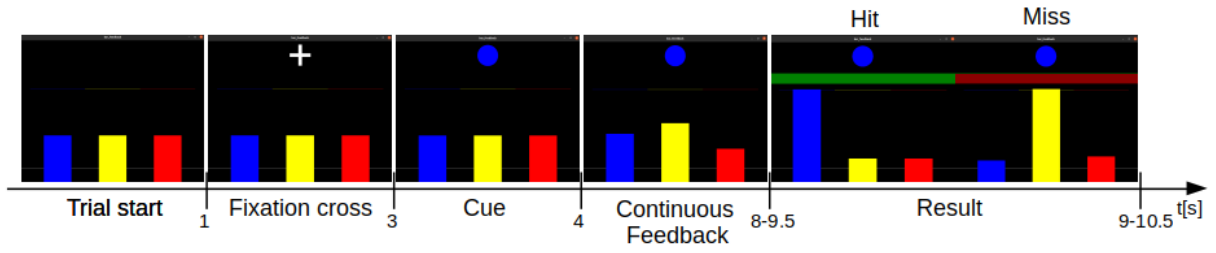
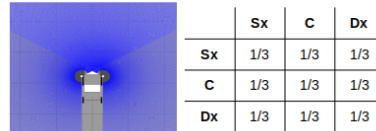


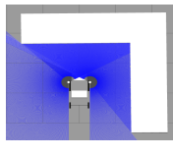
Figure 2.9: Trial design used for the evaluation runs, showing an example of 'Both Feet' trial. The visual feedback was drawn using the *neurodraw* ROS package. Each bar represents the probability assigned to each class after the exponential smoothing. When the bar corresponding to the cue ball's color reaches its threshold, a green horizontal bar appears, indicating the target was hit. Otherwise, a red bar signals that the target was missed.

T_{off} : constant equally probable transition matrix

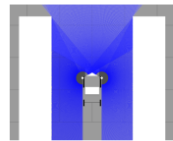


Both Feet (Sx), Rest (C), Both Hands (Dx)

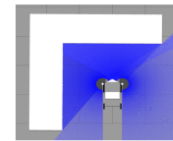
T_1 : only the direction for the cue task is open



Both Feet (Sx)

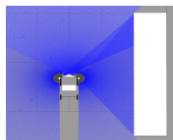


Rest (C)

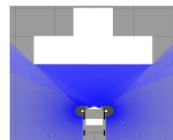


Both Hands (Dx)

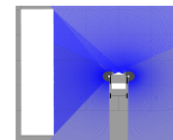
T_2 : one additional direction is open beside the one for the cue task



Both Feet (Sx), Rest (C)



Both Feet (Sx), Both Hands (Dx)



Rest (C), Both Hands (Dx)

Figure 2.10: Obstacles spawned during the three evaluation types. Beside and below each picture the resulting transition matrix and the trial classes are provided respectively. During the T_{off} modality a constant equally probable matrix was used to access the basic function of the pipeline without the traversability help. Instead, during T_1 and T_2 modalities the traversability system was exploited in order to generate the time varying transition matrix encoding information about the surroundings, and therefore helping in the classification. While T_{off} corresponds to *no help* from the system, T_1 corresponds to a *low help* level, and T_2 to an *high help* degree.

3 Results

The results were computed over the data collected from six healthy subjects that took part in the evaluation procedure. These subjects featured different levels of experience with the BCI and were almost the same age, from 23 to 26 years old. In particular two proficiency and one intermediate subjects participated to four complete acquisitions each, while the other three novelty subjects took part in only one complete acquisition each. Table 3.1 resumes all the subjects details. During the first acquisition the subject had to perform 3 calibration runs in order to collect enough data and train the binary Gaussian classifier. Then, a first evaluation on only the two classes, 'Both Hands' and 'Both Feet', were acquired every subsequent sessions to assess the effectiveness of the classifier and the stability of the selected features. Ulterior calibration runs were acquired only if the classifier needed to be updated due to poor control performances. Finally, 6 3-classes evaluation runs, 2 runs per modality (T_{off} , T_1 , T_2), were acquired using a random order for assessing the effectiveness of the HMM system. For both calibration and evaluation runs the task were randomized for a total of 10 trial per class. Table 3.2 reports the runs type along a typical acquisition. Confusion matrix and accuracy were computed on the data collected from the 3-classes evaluations in order to assess the effectiveness of the proposed framework.

Subject	Experience Level	Gender	Age	Status	N Acquisitions	N Classifier Update
C7	Proficiency	M	25	Healthy	4	3
D6	Proficiency	M	26	Healthy	4	2
G2	Intermediate	M	26	Healthy	4	2
H5	Novelty	F	23	Healthy	1	1
H6	Novelty	F	23	Healthy	1	1
H7	Novelty	M	23	Healthy	1	1

Table 3.1: Subjects details

	Calibration	Binary evaluation	T_{off}	T_1	T_2
N runs	3	1	2	2	2
N trial	30	20		30	
N trial per class	10	10		10	
Duration per run	4min	2.5min		5min	

Table 3.2: Acquisition details

3.1 Real Task Distributions

As mentioned in the section 2.4.2 the HMM states were designed based on the expected probability distribution of the classifier output, but after collecting real data it was possible to notice clear differences between the ideal and the real distributions. In particular, the binary Gaussian classifier used in the project is characterized by an erratic behavior, meaning that when the subject is asked to perform one of the two active tasks ('Both Hands' and 'Both Feet'), the probability output may fluctuate between 0 and 1, leading to a probability distribution that is more prevalent around 1, but presenting a peak also in 0 [33]. As a consequence, if the erratic behavior is prevalent for one of the two active task, that task can be easily misclassified as 'Rest' class. In addition, the real distribution of the 'Rest' class was not always evenly split between 0 and 1, often showing a polarization toward either 0 or 1. This behavior could lead to misclassifications between the 'Rest' class and the class toward which the polarization occurred. Furthermore, if the subject did not show reliable features, namely with low discriminant power, the distribution for all the classes tend to be flatten or concentrated around 0.5, leading to poor classification performances. As follow, some example of real distributions are shown. In particular, the figures show the probability distribution of the classifier output for each class ('Both Feet', 'Rest', 'Both Hands') related to the 'Both Feet' output retrieved during one of the the T_{off} evaluation, which was not influenced by the varying transition matrix.

As it is possible to notice from the Figure 3.1, the subject C7 showed a distribution for the 'Rest' class similar to the ideal one with only a slight polarization, while the distribution for the 'Both Feet' and 'Both Hands' classes were characterized by the typical erratic behavior previously described, featuring a clear peak in 0 and 1 respectively. As a consequence, during the respective acquisition, the 'Both Feet' class was missclassified as 'Rest' class 6 times out of 20, and the 'Rest' class showed an unstable behavior, not being able to reach the needed threshold 14 times out of 20. The confusion matrix for this specific acquisition is also provided in the same figure.

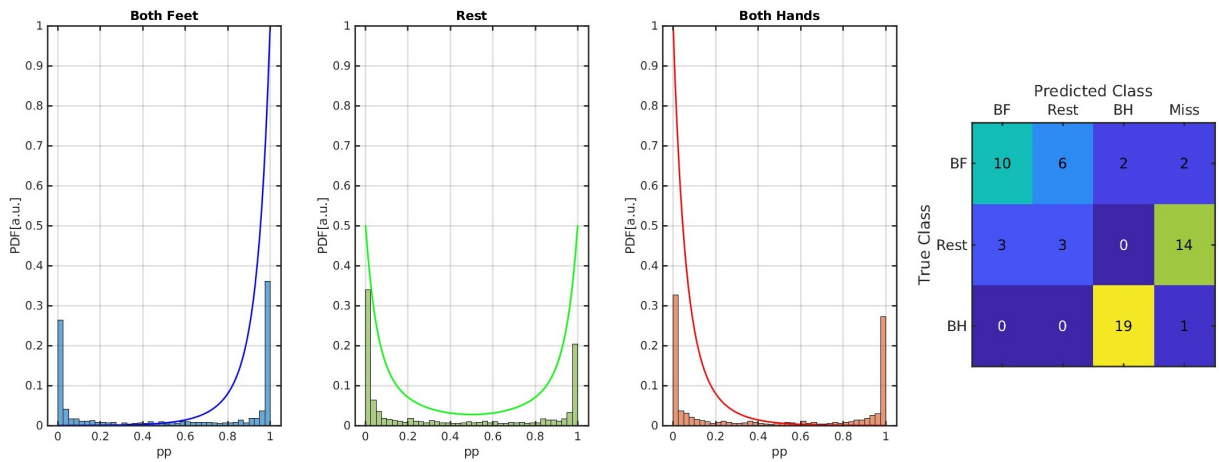


Figure 3.1: Subject C7: T_{off} distributions (left) and resulting confusion matrix (right) for a single acquisition. The 'Both Feet' and 'Both Hands' classes show the typical erratic behavior that characterizes the employed Gaussian classifier, causing instability in the classification of 'Both Feet' and 'Rest' classes.

Subject D6 also showed distributions different for the ideal one, as provided in Figure 3.2. In this case the 'Rest' class distribution was characterized by a strong polarization toward the 'Both Feet' class, leading to both the misclassification of the 'Rest' class as 'Both Feet' class 9 times out of 20, and an unstable behavior of the same class that was missed 10 times out of 20. Furthermore, it is possible to notice a strong erratic polarization in the distribution of the 'Both Hands' class, which however did not effected the accuracy in hitting both the 'Both Hands' and the 'Both Feet' classes that were correctly classified 17 and 19 times out of 20 respectively, as shown in the relative confusion matrix.

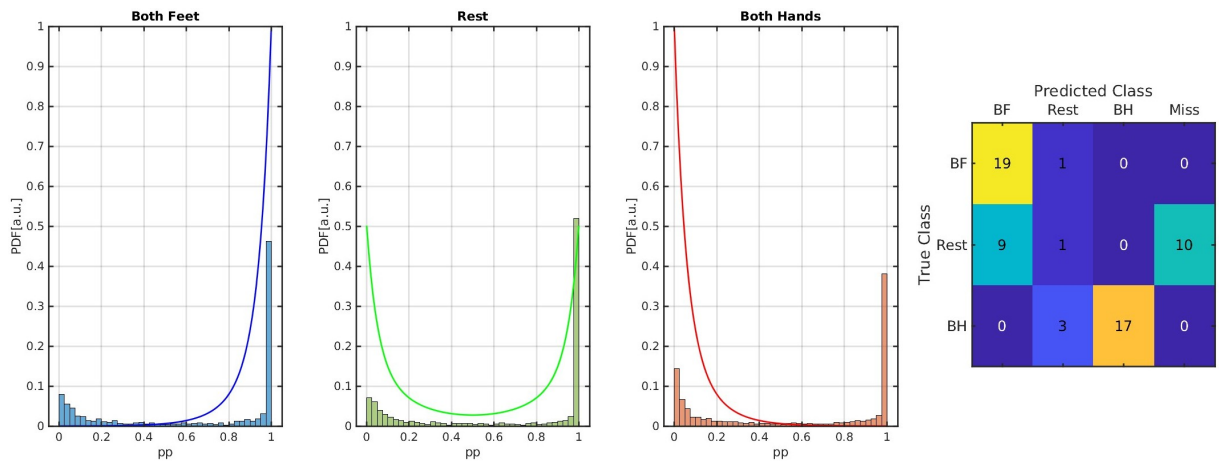


Figure 3.2: Subject D6: T_{off} distributions (left) and resulting confusion matrix (right) for a single acquisition. The 'Rest' class shows a strong polarization toward the 'Both Feet' class, leading to instability in the classification of the same class.

Figure 3.3 shows the distributions for the subject G2. In this case the intermediate subject showed a similar distribution for all the three classes, lacking of the expected polarization toward 0 for the 'Both Hands' class, and showing a heavily polarized distribution toward 1 for the 'Rest' class. This led to poor accuracy for the 'Rest' and 'Both Hands' classes that were correctly classified only 9 times and 5 times out of 20 respectively. The problem did not occur for the 'Both Feet' class, as it is possible to learn from the relative confusion matrix.

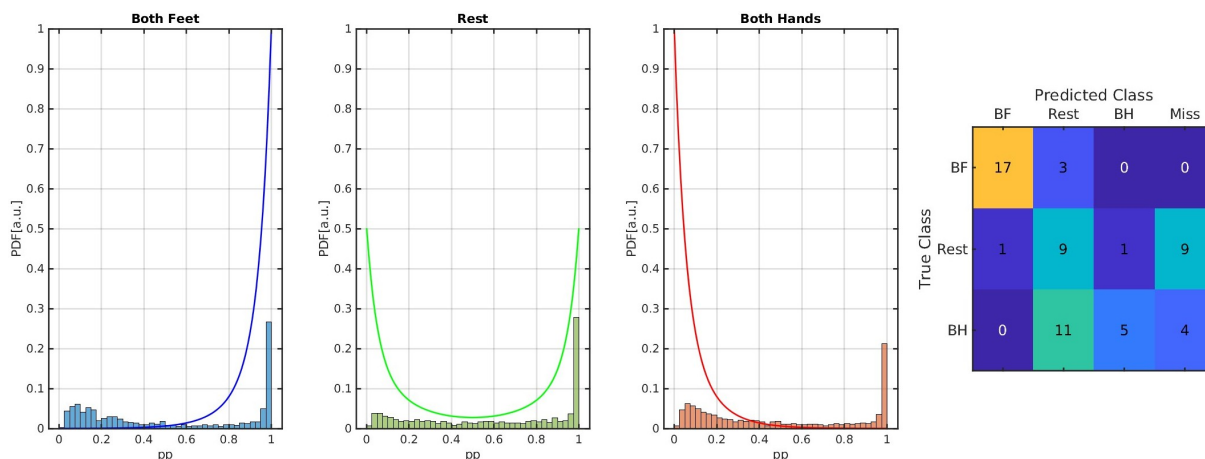


Figure 3.3: Subject G2: T_{off} distributions (left) and resulting confusion matrix (right) for a single acquisition. The 'Both Hands' class lacks of the expected peak in 0 while the 'Rest' is polarized toward 1. This led to poor discriminability between the cited classes.

Figure 3.4 display the distribution obtained from the novelty subject H5. In this case the subject showed weak features that led the distributions to be flatten, without the usual peaks in 0 and 1, in addition the distribution of 'Both Hands' class seems to be polarized toward 1 instead of 0. As a result, the subject experienced poor control capabilities, not being able to perform the 'Both Hands' class, that was mistaken for the other two classes. As it is possible to notice from the resulting confusion matrix shown in the same figure, also the 'Both Feet' and 'Rest' classes were classified almost by chance, showing a general misclassification behavior.

An other clear example of consequences of weak features is provided in Figure 3.5, were the distributions for the subject H6 are shown. In this case the subject was not able to elicit useful features in order to perform a proper control, indeed, as also provided in the confusion matrix, the proposed framework classified all the trial as 'Rest' class.

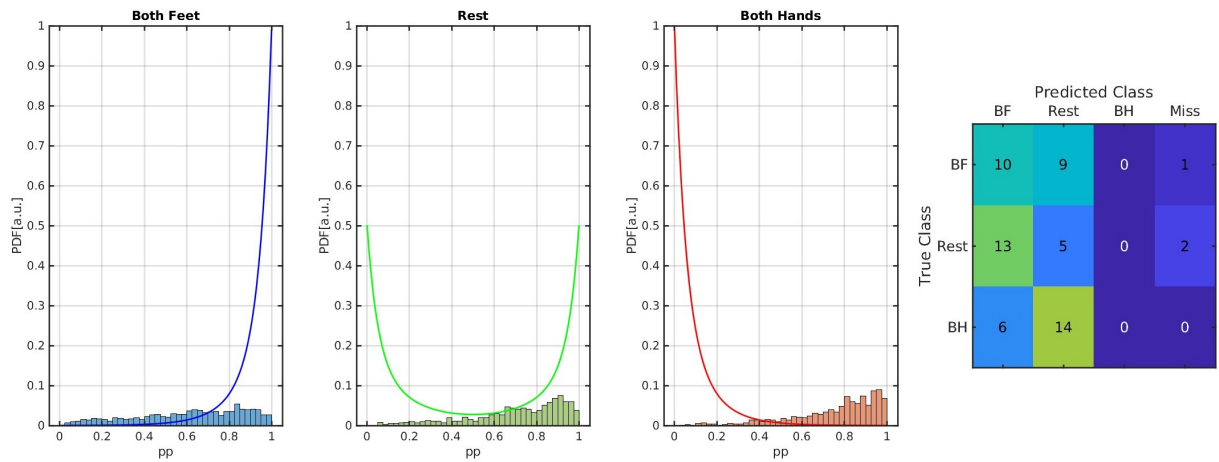


Figure 3.4: Subject H5: distributions (left) and resulting confusion matrix (right) for the T_{off} runs. Due to poor features, the distributions appear to be flattened, leading to low control capabilities.

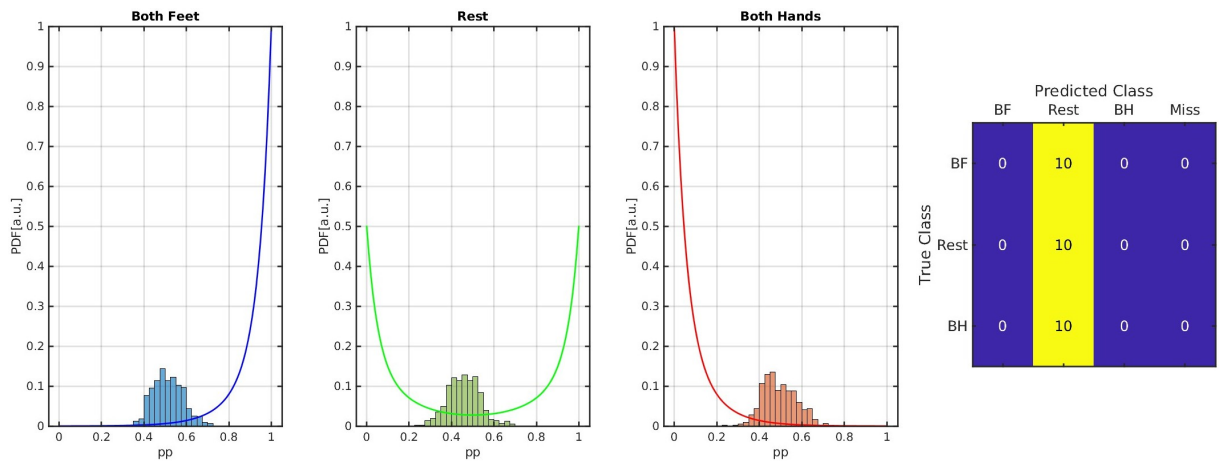


Figure 3.5: Subject H6: distributions (left) and resulting confusion matrix (right) for the T_{off} runs. All the trials were classified as 'Rest' due to the absence of control capabilities.

Contrary, the novelty subject H7 showed relatively consistent features which brought to the distribution showed in Figure 3.6. It is possible to notice that both 'Both Feet' and 'Both Hands' class feature the erratic behavior also shown for the subject C7, with the difference that in this case the peaks in 0 and 1 are smaller. Furthermore, the 'Rest' class distribution seems to be slightly polarized toward 1. As a result the 'Both Hands' class was misclassified as 'Rest' class 12 times out of 20, and the 'Rest' showed unstable behavior being misclassified as 'Both Feet' class 8 times out of 20, as it is provided in the confusion matrix.

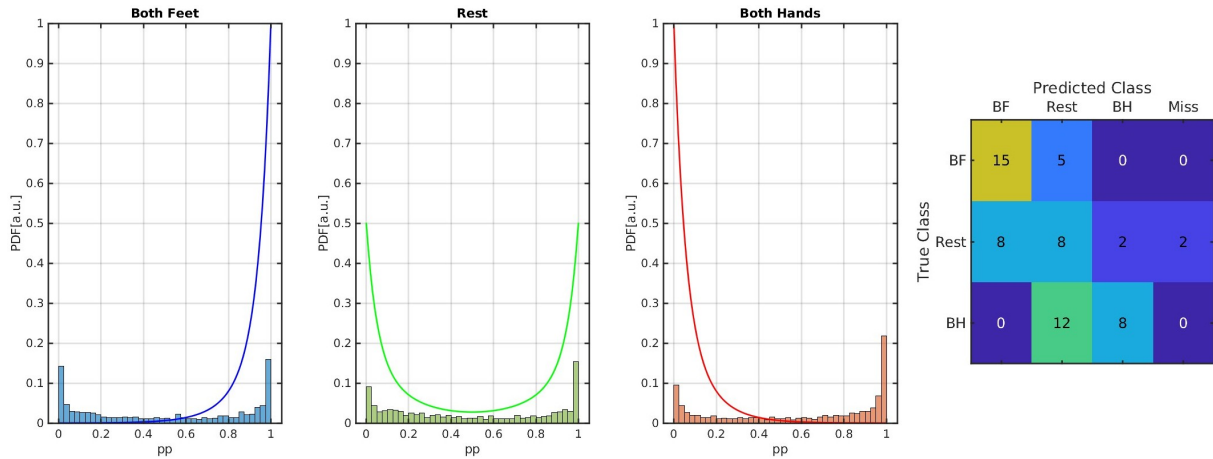


Figure 3.6: Subject H6: distributions (left) and resulting confusion matrix (right) for the T_{off} runs. The subject showed modest control capabilities. Due to the erratic behavior a low accuracy was recorded for both the 'Rest' and 'Both Hands' class.

It is important to mention that the displayed distributions for the subjects C7, D6, and G2 are derived from a single complete acquisition. However, in the other three acquisitions, the distributions exhibited similar patterns to the ones provided. This suggest that the shapes of the distributions are intrinsic characteristic of the subject in case of strong and stable features. An extended explanation about the reasons why the HMM states were designed after the ideal distributions and not the real and subject specific ones is provided in the Discussion chapter at page 47.

3.2 Performance and Traversability Effects

Thanks to the data collected, it was possible to prove how using the HMM transition matrix for incorporating the environmental information into the classification process led to enhanced performances in the T_1 (*low help*) and T_2 (*high help*) evaluation runs compared to the T_{off} (*no help*) one. Indeed, subject C7 achieved an average overall accuracy across the runs of $51.67 \pm 9.59 \%$ in the T_{off} modality, $59.58 \pm 9.50 \%$ in T_1 , and $69.17 \pm 14.34 \%$ in T_2 , experiencing an improvement of 17.5% in the latter modality compared to the first one. Subjects D6 and G2 also showed significant improvement in overall accuracy in the T_2 (*high help*) modality compared to the T_{off} one. They were able to achieve average overall accuracies of $75.71 \pm 7.53 \%$ and $69.58 \pm 5.76 \%$ respectively, recording an average improvement of 20.28% and 19.58% over the T_{off} results. Also the novelty subject H7 experienced boosted accuracy for the assisted evaluation runs, T_1 and T_2 , going from an average overall accuracy of $51.67 \pm 8.33 \%$ in T_{off} , to 61 ± 11.67 in T_1 , and $81.67 \pm 11.67 \%$ in T_2 . All the subjects that showed good control capabilities reported that was easier and more comfortable controlling the visual feedback during T_1 and

especially during T_2 evaluation modality, in which they managed to reach accuracy peaks even over 90 %. As it is possible to notice from the confusion matrix in Figures 3.7-3.8-3.9-3.10, the integration of the environment information into the transition matrix of the HMM significantly improved the class specific accuracy especially in the T_2 modality. The novelty subject H5 also exhibited enhanced performance in the T_1 and T_2 modalities. Despite presenting poor features and being unable to move the cursor in the binary evaluation feedback, the proposed framework showed improvements. Although she was not able to move the cursor for the 'Both Hands' task, the introduction of the traversability system led to accurate classification of the 'Both Feet' class against the other two classes, and vice versa, as shown in Figure 3.11. This was not the case for subject H6, who was unable to control the visual feedback even during the assisted evaluation, resulting in all trials being classified as the 'Rest' class.

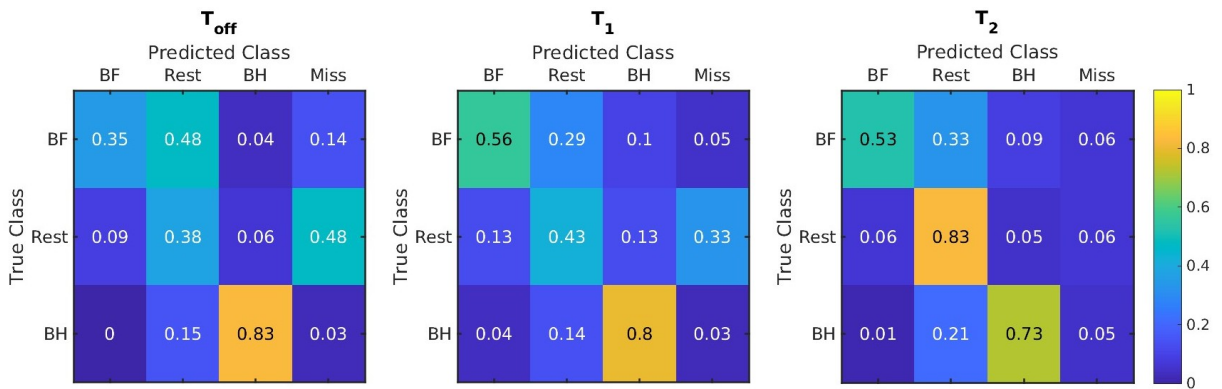


Figure 3.7: Subject C7. For each evaluation modality the confusion matrix averaged across the acquisitions is shown. Percentage values are used. BF stands for 'Both Feet', while BH stands for 'Both Hands'.

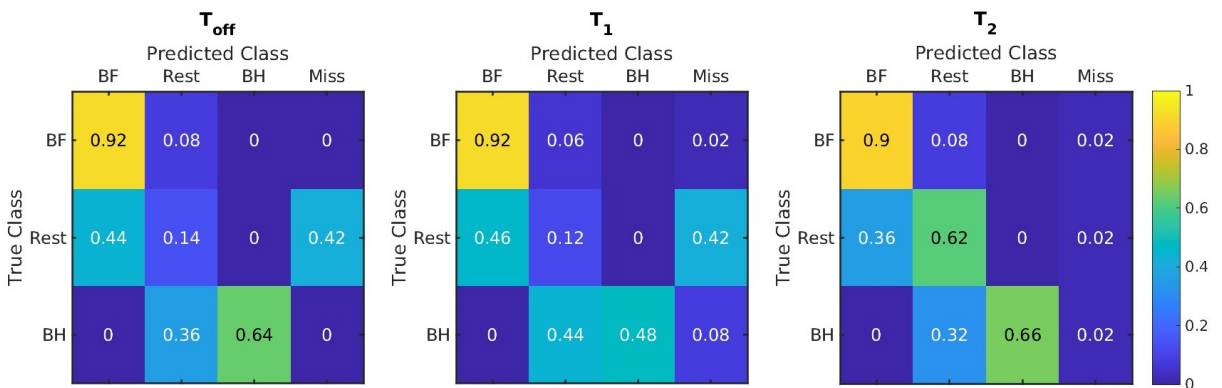


Figure 3.8: Subject D6. For each evaluation modality the confusion matrix averaged across the acquisitions is shown. Percentage values are used. BF stands for 'Both Feet', while BH stands for 'Both Hands'.

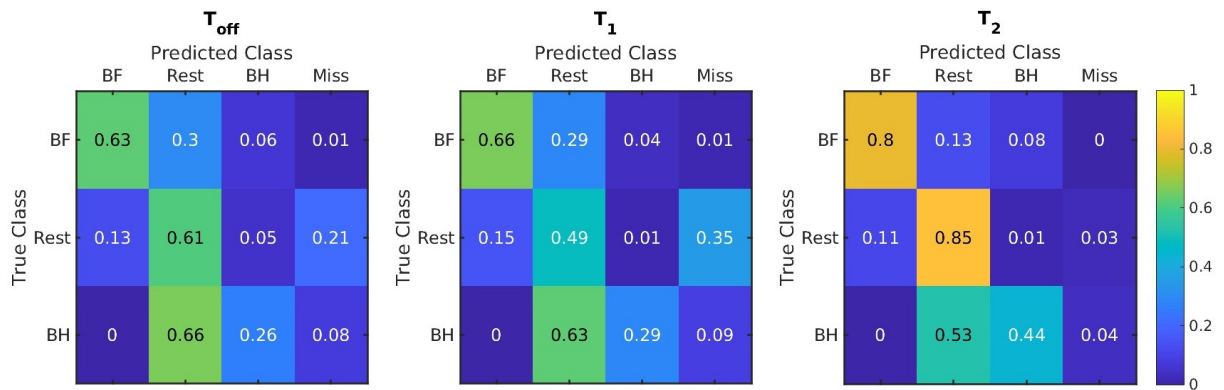


Figure 3.9: Subject G2. For each evaluation modality the confusion matrix averaged across the acquisitions is shown. Percentage values are used. BF stands for 'Both Feet', while BH stands for 'Both Hands'.

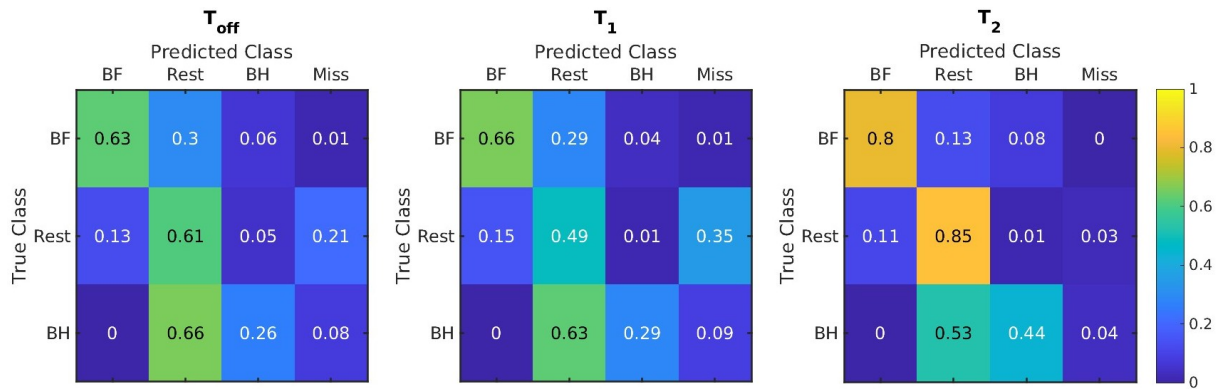


Figure 3.10: Subject H7. For each evaluation modality the confusion matrix is shown. Percentage values are used. BF stands for 'Both Feet', while BH stands for 'Both Hands'.

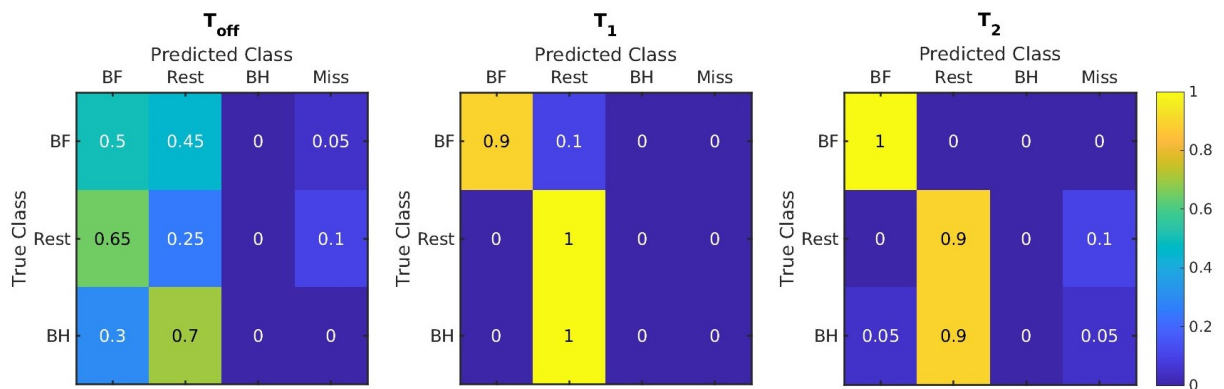


Figure 3.11: Subject H5. For each evaluation modality the confusion matrix is shown. Percentage values are used. BF stands for 'Both Feet', while BH stands for 'Both Hands'.

Therefore, all the subjects, excluding H6, experienced enhanced performances thanks to the integration of the environmental data into the classification process. Considering the overall accuracy averaged across the subjects, starting from 50.18 ± 10.32 % in the T_{off} (*no help*) evaluation runs, it was recorded a general improvement till 55.08 ± 9.76 % in the T_1 (*low help*) evaluation modality, and a further enhancement reaching 71.98 ± 9.65 % in the T_2 (*high help*) evaluation runs, as it is shown in Figure 3.12. Thus, an average improvement of 5 % and 21.7 % was recorded for the T_1 and T_2 evaluation modality respectively, compared to the T_{off} one, which, however, still above the chance level of 33.3 % in terms of overall accuracy. The statistical significance of these increments has been assessed through out the T-test, leading to the conclusion that, although the T_1 modality did not show a statistical significant improvement in the overall accuracy, with a p-value of 0.11, the enhanced performances recorded for the T_2 modality were statistical significant with p-values of 3.68×10^{-10} and 9.46×10^{-7} compared to the T_{off} and T_1 modality respectively.

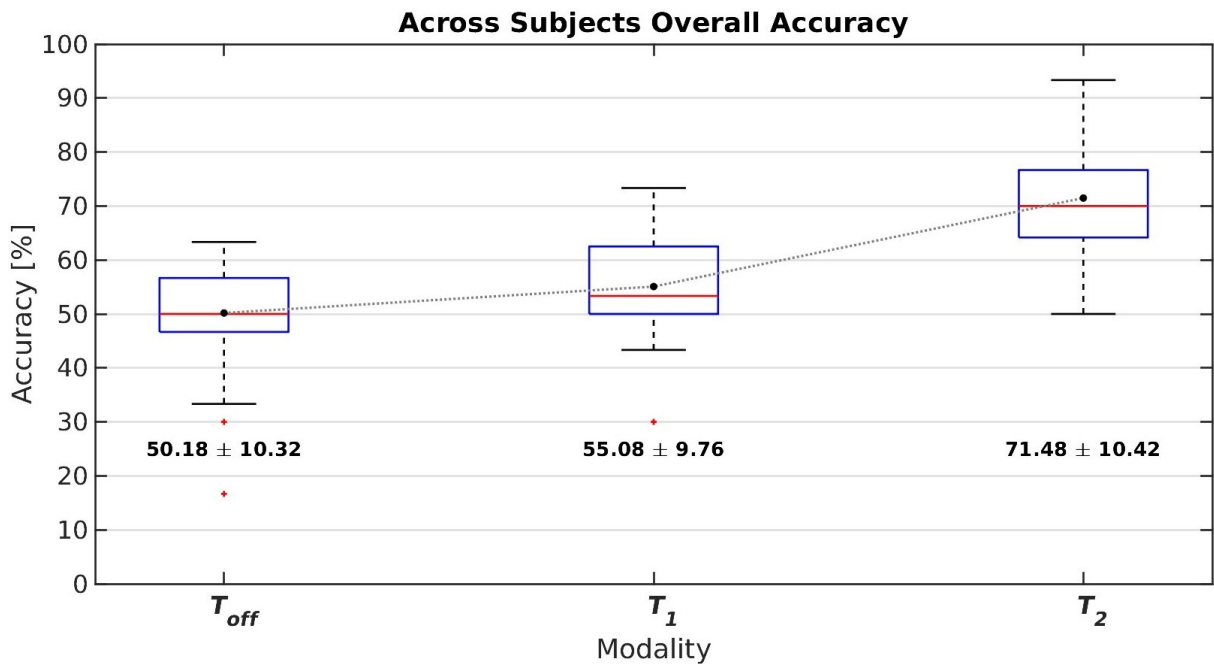


Figure 3.12: Box-plot of the overall accuracy across the subjects for each 3-classes evaluation modalities: T_{off} (*no help*), T_1 (*low help*), and T_2 (*high help*). Superimposed to the graph the average accuracy for each modality is shown.

4 Discussion

In this thesis a novel implementation of the Hidden Markov Model (HMM) was applied to an already existing Motor Imagery (MI) based BCI, which was previously used for driving an electrical wheelchair, in order to fulfill two main goals. First, to extract an additional 'Rest' class, along side the 'Both Feet' and 'Both Hands' classes, interpreting the probability output of the binary classifier. Second, under the hypothesis that the probability of performing one task depends on the surrounding, the system was designed to incorporate the environmental information prior the actual classification in order to help the end user taking the right decision. Figure 4.1 resumes the pipeline employed in this study.

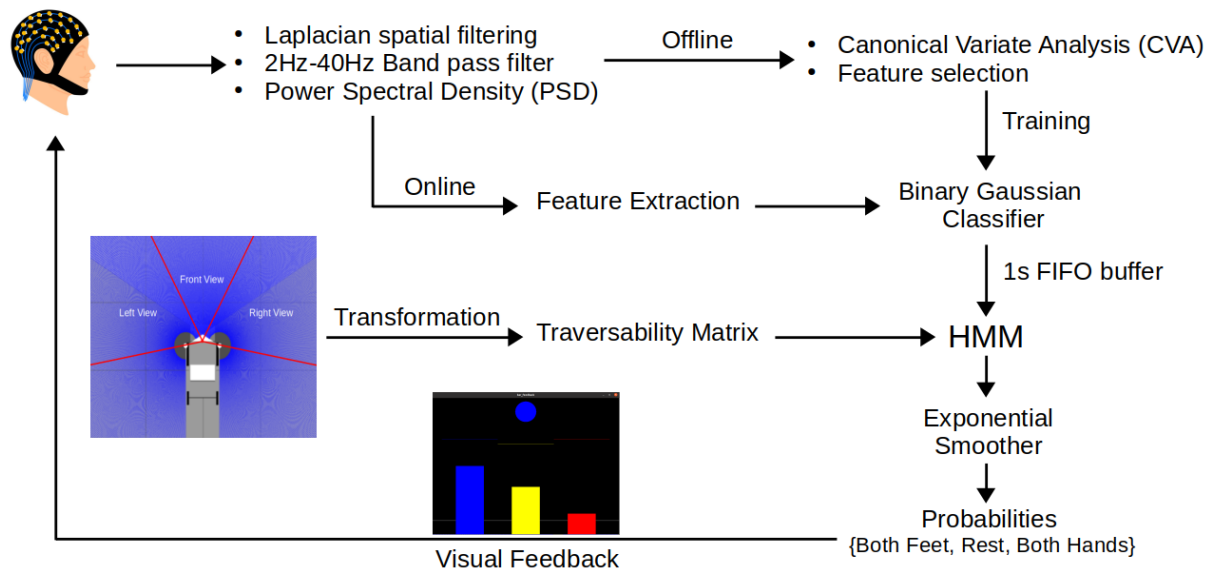


Figure 4.1: BCI pipeline employed in this study. The 16-channel EEG was retrieved from the subject scalp, then the signal was processed in order to extract the PSD. First, during the Offline phase, the most discriminant feature were selected through out CVA, and the binary Gaussian classifier was trained up on the calibration data. Consequently, during the Online phase, the output of the classifier was accumulated in a 1 second long FIFO buffer and interpreted by the HMM, whose transition matrix was built based on the environmental information. Then, the raw HMM output was low-pass filtered by the exponential smoother in order to obtain the final probability per class. An ad-hoc visual feedback was employed to close the BCI loop.

Thanks to the Hidden Markov Model framework it was possible to consider each task as a state, which depends on the raw probability output of the binary Gaussian classifier, forming a fully connected net of three states, namely, 'Both Feet', 'Rest', and 'Both Hands'. The transition between these state was ruled by a transition matrix, which was the output of the surrounding environment analysis.

The PDFs that featured each state were designed based on the ideal raw probability distribution of the 'Both Feet' class. While 'Both Feet' and 'Both Hands' classes were characterized by mirrored PDFs, the 'Rest' class PDF was not the mere mean between these two. Indeed, in order to consider raw probability sample around 0.5 more strongly belonging to the 'Rest' class, the PDF was the mean between a less steep version of the PDF of the other two classes. However, from the results, it is evident that these PDFs did not accurately represent the real probability distributions. In fact, they failed in describing the subject specific distribution which often involved the erratic behavior typical of the Gaussian classifier. Despite this, using this method was the most suitable solution available for interpreting the raw output of the classifier and retrieve the three classes out of the original two. Indeed, employing PDFs fitted on the real distributions, such as gamma, log-gamma, or beta functions, would have led to highly overlapped and similar PDFs functions across the classes. Consequently, during the forward algorithm, the posterior likelihood values for the samples would have been too close across the classes, leading to extremely low discriminative power. Furthermore, when the subject is asked to perform one of the two original classes, for example the reference class, it is reasonable to expect that higher probability values close to 1 correspond to higher likelihood values on the reference class PDF. However, there is no reason for considering erratic values, namely, probability values close to 0, as belonging to the same class. As a result, using ideal instead of fitted PDFs lead to higher probability of belonging to one of the two original classes, 'Both Hands' and 'Both Feet', only if the raw classification was correctly polarized toward 0 or 1 respectively, otherwise the sample was considered to belong to one of the other two classes. In order to restrain the effect of this erratic behavior on the final classification two methods were used simultaneously: prior the classification, the posterior likelihood is computed over a 1 second long buffer of raw probability samples in order to capture the overall likelihood over 16 samples and not only the likelihood of a single sample; afterward the classification, the exponential smoother works as evidence collector, slowing down the changes in the final classes probability.

The method used for computing the transition matrix took into account only the total occupancy over bounded areas of the cited *costmap_2d* matrix. Therefore, the central row of the transition matrix could be interpreted as the probability for each direction to be free of obstacles compared to the others. This means that if the three directions were equally occupied, the resulting

probability would have been equal across the directions as well. For this reason during the T_1 evaluation run, which involved only one direction to be free of obstacles, the closed directions did not feature extremely low probability as might have been expected, since they shared the probability to be occupied. As a consequence, only a mild level of assistance was delivered to the subject in performing the right choice. Instead, during the T_2 evaluation modality, only one direction was blocked, while the other two were completely clear. This means that the only blocked direction featured an extremely high occupancy level compared to the other two, leading to an almost zero probability in the resulting transition matrix. As a result, this modality offered a high level of assistance to the end user, making almost impossible to choose the blocked direction.

Promising results have been shown despite the highlighted limitations, supporting the idea that further improvements of the proposed framework would lead to enhanced outcomes. For example the HMM states could be designed directly over the distributions of the most discriminant features across the three classes, avoiding the need to interpret the probability output of the binary classifier. In this way, the HMM would be fed directly with the PSD samples of the chosen features, working as a 3-classes classifier itself. In addition, further implementations of the Traversability system could lead to a more effective integration of the environmental data into the framework for better assisting the user in performing the right task. Alongside the methods for incorporating the surrounding information prior the classification, refined computer vision algorithms could be involved in the posterior process of interpreting the user intentions in order to build a complete semi-autonomous shared controlled system. Thanks to this technology it would be possible not only to help the end user in making the right choice, but also understand the subjects needs and, based on them, autonomously drive the wheelchair. As it is shown also from the data collected in this study, Motor Imagery skills can sometimes be innate, as in the case of the subject H7, however, in most cases, the subjects require specific training in order to develop such features, and despite that, improvements are not guaranteed. For this reason, refining shared-control systems could broaden the accessibility of BCI driven assistive devices to those with minimal training, ensuring a remarkable improvement in life quality.

In conclusion, this thesis aimed to contribute to the research in shared-control BCI by presenting a novel implementation of the Hidden Markov Model for a BCI driven wheelchair. The hope is that this framework can pave the way for further advancements and effective solutions, ultimately improving the quality of life for those who rely on such assistive technologies.

A Appendix

A.1 Hidden Markov Model Foundation

Hidden Markov Models (HMMs) are highly versatile and have found widespread applications across various fields due to their ability to model sequential data with hidden states [34]. In speech recognition, HMMs are used to link audio signals with underlying phoneme sequences, enabling both speaker-independent and continuous recognition [34]. They also play a significant role in natural language processing tasks like part-of-speech tagging and machine translation [34]. In bioinformatics, HMMs are useful for predicting protein structures, aligning DNA sequences, and identifying genes [34]. In finance, they model time-series data for stock prediction and risk management [34]. HMMs are equally useful in human activity recognition, robotics, and video analysis, where they track movements and predict behaviors. Moreover, HMM variants such as higher-order HMMs (HO-HMM), hidden semi-Markov models (HSMM), and hierarchical HMMs (HHMM) expand their applicability, improving modeling in fields like machine health monitoring, weather forecasting, and even cybersecurity [34]. This interdisciplinary adaptability makes HMMs an important tool in several scientific, technical, and industrial domains [34].

The HMM is a tool derived from the Bayesian Network theory. In particular, the latter one is a graphical method useful for representing conditional independencies between a set of random variables, providing the view of a particular joint distribution factorization [35]. When Bayesian Networks are applied to time series data, they are referred to as Dynamic Bayesian Networks (DBN). These models are based on the assumption that events in the present can be caused or influenced only by past events [35]. In this context, DBNs are particularly effective for modeling finite state machines, which represent stochastic processes involving a finite number of states or events, regularly spaced in discrete time intervals. The transitions between these states are determined by probabilities that depend on the states at the previous time points [35]. This particular process takes the name of first order Markov Chain (MC) when the following properties are respected:

- The process is defined as discrete time series of states q_t , which can take finite number of values from 1 to N [36].
- The state at instant t_i depends only on the event at the previous instant t_{i-1} , namely, the model is compliant with the Markov property [36].
- The transition probabilities are described by the transition matrix $A = \{a_{ij}\}$, where a_{ij} is the probability to jump from state $q_t = S_i$ to state $q_{t+1} = S_j$. Thanks to the Markov property it can be defined as $a_{ij} = P(q_t = S_j | q_{t-1} = S_i)$. Since it is a probability $a_{ij} \geq 0 \forall i, j \in [1, N]$ and $\sum_{j=1}^N (a_{ij}) = 1$ [36].
- The initial probability of being at state S_i is denoted as $\pi_i = P(q_1 = S_i)$, forming the vector $\Pi = [\pi_1, \pi_2, \dots, \pi_N]$ [36].

Markov Chains are also called Observable Markov Model since each state correspond to a directly observable and visible event.

Finally, the Hidden Markov Model (HMM) is an extension of the Markov Chain concept. In particular the states involved in the series are hidden from the observer, who can only retrieve observations about the current state. Indeed, beside the probability for each state to occur in the series, each state has also different probabilities to emit a certain observation, and for this reason HMMs are considered doubly stochastic process [35][36]. Thus, HMMs share the basic properties of the MC, but in addition:

- The N $q_t \in \{S_1, S_2, \dots, S_N\}$ different states involved in the model are hidden and not directly accessible by the observer [36].
- Each state can take M distinct observations $O_t \in \{o_1, o_2, \dots, o_M\}$. The probability of each state to emit a certain observation is described by the observation probability distribution $B = \{b_i(k)\} = P[O_t = o_k | q_t = S_i]$, where $b_i(k)$ is the probability to witness the observation o_k given that the current state is S_i , with $k \in [1, M]$ and $i \in [1, N]$ [36].

Therefore the HMM is fully described when the state transition matrix A , the observation probability distribution B , and the initial state distribution Π are known. The HMM($\lambda(A, B, \Pi)$), so defined generates an observation sequence $O = \{O_1, O_2, \dots, O_T\}$ over time [36]. An example of HMM is provided in Figure A.1.

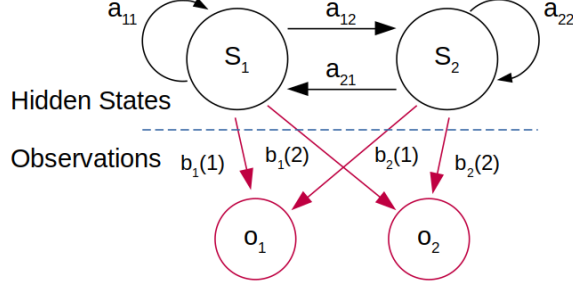


Figure A.1: Scheme of an HMM consisting of 2 hidden states (S_1, S_2) and 2 possible observations for state (o_1, o_2). The transition between the hidden states is ruled by the transition matrix $A = \{a_{ij}\}$, while the observation emission probability is described by $B = \{b_i(k)\}$.

A.1.1 Forward Algorithm

The Forward algorithm is a dynamic programming approach for solving the so called "likelihood problem", namely for computing the probability of observing a particular sequence of observation given the model parameters [36]. Thanks to this recurrent method, instead of computing the joint probability between the observations sequence and all the possible combinations of states, the complexity lower from $O(2TN^T)$ to $O(TN^2)$, where T is the length of the sequence and N is the number of hidden states [36]. The Forward algorithm is based on the computation of $\alpha_t(i) = P(O, q_t = S_i | \lambda)$, namely the probability that, given the model parameters λ , the last state $q_t = S_i$ gives the observation o_t after the observation sequence o_1, o_2, \dots, o_{t-1} . The algorithm proceeds through out inductive steps as follow.

- First step:

$$\alpha_1(i) = \pi_i \times b_i(o_1) \quad \text{with} \quad i \in [1, N] \quad (\text{A.1})$$

where π_i is the initial probability for the hidden state i , while $b_i(o_1)$ is the probability for the state i to emit the observation o_1 as first observation of the sequence [36].

- Inductive step:

$$\alpha_t(j) = b_j(o_t) \times \sum_{i=1}^N (\alpha_{t-1}(i) \times a_{ij}) \quad \text{with} \quad j \in [1, N], t \in [1, T] \quad (\text{A.2})$$

where $b_j(o_t)$ is the probability for the state j to emit the observation o_t at the current step, $\alpha_{t-1}(i)$ is the likelihood from the previous step for the state i , and a_{ij} is the transition probability between the states i and j [36]. Notice that for long sequences α_t become vanishingly small as the recursion progress, therefore a normalization to sum to one is performed at each step [35].

- In conclusion:

$$P(O | \lambda) = \sum_{i=1}^N (\alpha_T(i)) \quad (\text{A.3})$$

represent the cumulative likelihood along the sequence, namely the probability of witnessing a particular observation sequence given the model parameter λ .

A.1.2 Other Algorithms

Other algorithms have been refined in order to solve further questions on the HMM. Indeed, similarly to the Forward algorithm, through out the Backward algorithm is possible to compute the element $\beta_t(i) = P(O_{t+1}, O_{t+2}, \dots, O_T) | q_t = S_i, \lambda$, namely the probability to register a particular partial observations sequence starting from the instant t , given the initial state S_i and the model parameters λ [36]. In addition, the Viterbi algorithm once again exploits dynamic programming in order to recursively retrieve the probability of being in a state S_i at a time t based on the most probable path that leads to that state. Tracking all the most probable state at each time step, the Viterbi algorithm allows to compute the most likely sequence of state that generated the given sequence of observations [36]. All the algorithms introduced so far relied on known model parameters $\lambda(A, B, \Pi)$, contrary, the Baum-Welch algorithm aims to estimate such parameters given a sequence of observations. This particular algorithm is based on the Expectation and Maximization method, thanks which, starting from some initial values, the model parameters are iteratively updated using the results from the Forward and Backward algorithms till a stable point is reached [36][35].

Bibliography

- [1] J. J. Vidal, “Toward direct brain-computer communication,” *Annual review of Biophysics and Bioengineering*, vol. 2, no. 1, pp. 157–180, 1973. doi: <https://doi.org/10.1146/annurev.bb.02.060173.001105>.
- [2] A. Kübler, “The history of bci: From a vision for the future to real support for personhood in people with locked-in syndrome,” *Neuroethics*, vol. 13, no. 2, pp. 163–180, 2020. doi: <https://doi.org/10.1007/s12152-019-09409-4>.
- [3] L. Tonin and J. d. R. Millán, “Noninvasive brain–machine interfaces for robotic devices,” *Annual Review of Control, Robotics, and Autonomous Systems*, vol. 4, no. 1, pp. 191–214, 2021. doi: <https://doi.org/10.1146/annurev-control-012720-093904>.
- [4] A. Rezeika, M. Benda, P. Stawicki, F. Gemblér, A. Saboor, and I. Volosyak, “Brain–computer interface spellers: A review,” *Brain sciences*, vol. 8, no. 4, p. 57, 2018. doi: <https://doi.org/10.3390/brainsci8040057>.
- [5] L. Tonin, S. Perdakis, T. D. Kuzu, *et al.*, “Learning to control a bmi-driven wheelchair for people with severe tetraplegia,” *Iscience*, vol. 25, no. 12, 2022. doi: <https://doi.org/10.1016/j.isci.2022.105418>.
- [6] R. M. Rothschild, “Neuroengineering tools/applications for bidirectional interfaces, brain–computer interfaces, and neuroprosthetic implants—a review of recent progress,” *Frontiers in neuroengineering*, vol. 3, p. 112, 2010. doi: <https://doi.org/10.3389/fneng.2010.00112>.
- [7] K. J. Miller, D. Hermes, and N. P. Staff, “The current state of electrocorticography-based brain–computer interfaces,” *Neurosurgical focus*, vol. 49, no. 1, E2, 2020. doi: <https://doi.org/10.3171/2020.4.FOCUS20185>.
- [8] M. Shokouejad, D.-W. Park, Y. H. Jung, *et al.*, “Progress in the field of micro-electrocorticography,” *Micromachines*, vol. 10, no. 1, p. 62, 2019. doi: <https://doi.org/10.3390/mi10010062>.

- [9] G. R. Müller-Putz, “Electroencephalography,” *Handbook of clinical neurology*, vol. 168, pp. 249–262, 2020. doi: <https://doi.org/10.1016/B978-0-444-63934-9.00018-4>.
- [10] D. U. Silverthorn, “Human physiology: An integrated approach,” *7th edition*, 2017.
- [11] J. W. C. Medithe and U. R. Nelakuditi, “Study of normal and abnormal eeg,” in *2016 3rd International Conference on Advanced Computing and Communication Systems (ICACCS)*, vol. 01, 2016, pp. 1–4. doi: [10.1109/ICACCS.2016.7586341](https://doi.org/10.1109/ICACCS.2016.7586341).
- [12] B. Blankertz, R. Tomioka, S. Lemm, M. Kawanabe, and K.-r. Muller, “Optimizing spatial filters for robust eeg single-trial analysis,” *IEEE Signal Processing Magazine*, vol. 25, no. 1, pp. 41–56, 2008. doi: [10.1109/MSP.2008.4408441](https://doi.org/10.1109/MSP.2008.4408441).
- [13] H. Altaheri, G. Muhammad, M. Alsulaiman, *et al.*, “Deep learning techniques for classification of electroencephalogram (eeg) motor imagery (mi) signals: A review,” *Neural Computing and Applications*, vol. 35, no. 20, pp. 14 681–14 722, 2023. doi: <https://doi.org/10.1007/s00521-021-06352-5>.
- [14] S. Aggarwal and N. Chugh, “Signal processing techniques for motor imagery brain computer interface: A review,” *Array*, vol. 1-2, p. 100 003, 2019, issn: 2590-0056. doi: <https://doi.org/10.1016/j.array.2019.100003>.
- [15] P. F. Diez, S. M. Torres Müller, V. A. Mut, *et al.*, “Commanding a robotic wheelchair with a high-frequency steady-state visual evoked potential based brain–computer interface,” *Medical Engineering & Physics*, vol. 35, no. 8, pp. 1155–1164, 2013, issn: 1350-4533. doi: <https://doi.org/10.1016/j.medengphy.2012.12.005>.
- [16] P. W. Ferrez and J. del R. Millan, “Error-related eeg potentials generated during simulated brain–computer interaction,” *IEEE Transactions on Biomedical Engineering*, vol. 55, no. 3, pp. 923–929, 2008. doi: [10.1109/TBME.2007.908083](https://doi.org/10.1109/TBME.2007.908083).
- [17] I. Iturrate, R. Chavarriaga, L. Montesano, J. Minguez, and J. d. R. Millán, “Teaching brain-machine interfaces as an alternative paradigm to neuroprosthetics control,” *Scientific reports*, vol. 5, no. 1, p. 13 893, 2015. doi: <https://doi.org/10.1038/srep13893>.
- [18] J. Höhne, M. Schreuder, B. Blankertz, and M. Tangermann, “A novel 9-class auditory erp paradigm driving a predictive text entry system,” *Frontiers in neuroscience*, vol. 5, p. 99, 2011. doi: <https://doi.org/10.3389/fnins.2011.00099>.
- [19] L. Tonin, R. Leeb, A. Sobolewski, and J Del R Millán, “An online eeg bci based on covert visuospatial attention in absence of exogenous stimulation,” *Journal of neural engineering*, vol. 10, no. 5, p. 056 007, 2013. doi: [10.1088/1741-2560/10/5/056007](https://doi.org/10.1088/1741-2560/10/5/056007).

- [20] L. Tonin, R. Leeb, and J Del R Millán, “Time-dependent approach for single trial classification of covert visuospatial attention,” *Journal of neural engineering*, vol. 9, no. 4, p. 045 011, 2012. doi: 10.1088/1741-2560/9/4/045011.
- [21] C. Jeunet, L. Tonin, L. Albert, *et al.*, “Uncovering eeg correlates of covert attention in soccer goalkeepers: Towards innovative sport training procedures,” *Scientific reports*, vol. 10, no. 1, p. 1705, 2020. doi: <https://doi.org/10.1038/s41598-020-58533-2>.
- [22] G. Pfurtscheller and F. Lopes da Silva, “Event-related eeg/meg synchronization and desynchronization: Basic principles,” *Clinical Neurophysiology*, vol. 110, no. 11, pp. 1842–1857, 1999, issn: 1388-2457. doi: [https://doi.org/10.1016/S1388-2457\(99\)00141-8](https://doi.org/10.1016/S1388-2457(99)00141-8).
- [23] L Leocani, C Toro, P Zhuang, C Gerloff, and M Hallett, “Event-related desynchronization in reaction time paradigms: A comparison with event-related potentials and corticospinal excitability,” *Clinical Neurophysiology*, vol. 112, no. 5, pp. 923–930, 2001, issn: 1388-2457. doi: [https://doi.org/10.1016/S1388-2457\(01\)00530-2](https://doi.org/10.1016/S1388-2457(01)00530-2).
- [24] M.-S. Vry, D. Saur, M. Rijntjes, *et al.*, “Ventral and dorsal fiber systems for imagined and executed movement,” *Experimental Brain Research*, vol. 219, pp. 203–216, 2012. doi: <https://doi.org/10.1007/s00221-012-3079-7>.
- [25] G. Pfurtscheller and C. Neuper, “Motor imagery and direct brain-computer communication,” *Proceedings of the IEEE*, vol. 89, no. 7, pp. 1123–1134, 2001. doi: 10.1109/5.939829.
- [26] B. J. Edelman, J. Meng, D. Suma, *et al.*, “Noninvasive neuroimaging enhances continuous neural tracking for robotic device control,” *Science robotics*, vol. 4, no. 31, eaaw6844, 2019. doi: <https://doi.org/10.1126/scirobotics.aaw6844>.
- [27] L. Tonin, T. Carlson, R. Leeb, and J. del R. Millán, “Brain-controlled telepresence robot by motor-disabled people,” in *2011 Annual International Conference of the IEEE Engineering in Medicine and Biology Society*, 2011, pp. 4227–4230. doi: 10.1109/IEMBS.2011.6091049.
- [28] G. Beraldo, S. Tortora, E. Menegatti, and L. Tonin, “Ros-neuro: Implementation of a closed-loop bmi based on motor imagery,” in *2020 IEEE International Conference on Systems, Man, and Cybernetics (SMC)*, 2020, pp. 2031–2037. doi: 10.1109/SMC42975.2020.9282968.
- [29] A. Schlögl, “Gdf-a general dataformat for biosignals,” *arXiv preprint cs/0608052*, 2006. doi: <https://doi.org/10.48550/arXiv.cs/0608052>.

- [30] D. J. McFarland, L. M. McCane, S. V. David, and J. R. Wolpaw, "Spatial filter selection for eeg-based communication," *Electroencephalography and Clinical Neurophysiology*, vol. 103, no. 3, pp. 386–394, 1997, issn: 0013-4694. doi: [https://doi.org/10.1016/S0013-4694\(97\)00022-2](https://doi.org/10.1016/S0013-4694(97)00022-2).
- [31] D.-J. Jwo, I.-H. Wu, and Y. Chang, "Windowing design and performance assessment for mitigation of spectrum leakage," in *E3S Web of Conferences*, EDP Sciences, vol. 94, 2019, p. 03 001. doi: <https://doi.org/10.1051/e3sconf/20199403001>.
- [32] F. Galan, P. W. Ferrez, F. Oliva, J. Guardia, and J. del R. Millan, "Feature extraction for multi-class bci using canonical variates analysis," in *2007 IEEE International Symposium on Intelligent Signal Processing*, 2007, pp. 1–6. doi: 10.1109/WISP.2007.4447615.
- [33] L. Tonin, F. C. Bauer, and J. del R. Millán, "The role of the control framework for continuous teleoperation of a brain–machine interface-driven mobile robot," *IEEE Transactions on Robotics*, vol. 36, no. 1, pp. 78–91, 2020. doi: 10.1109/TR0.2019.2943072.
- [34] B. Mor, S. Garhwal, and A. Kumar, "A systematic review of hidden markov models and their applications," *Archives of computational methods in engineering*, vol. 28, pp. 1429–1448, 2021. doi: <https://doi.org/10.1007/s11831-020-09422-4>.
- [35] Z. Ghahramani, "An introduction to hidden markov models and bayesian networks," *International journal of pattern recognition and artificial intelligence*, vol. 15, no. 01, pp. 9–42, 2001. doi: <https://doi.org/10.1142/S0218001401000836>.
- [36] Y. Khalifa, D. Mandic, and E. Sejdić, "A review of hidden markov models and recurrent neural networks for event detection and localization in biomedical signals," *Information Fusion*, vol. 69, pp. 52–72, 2021. doi: <https://doi.org/10.1016/j.inffus.2020.11.008>.